Modelling the impact of trapped lee waves on offshore wind farm power output

Sarah J. Ollier[1], Simon J. Watson[2]

[1]CREST – Loughborough University, Holywell Park, Loughborough LE11 3TU, UK
5 [2]Wind Energy Section, Faculty of Aerospace Engineering, Delft University of Technology, Kluyverweg 1, 2629 HS Delft, Netherlands.

Correspondence to: Sarah J Ollier (s.ollier@lboro.ac.uk)

Abstract. Mesoscale meteorological phenomena, including Atmospheric Gravity Waves~~, or~~ (AGWs), including Trapped Lee Waves (TLWs) can result from flow over topography or coastal transition in the presence of stable atmospheric stratification,
10 particularly with strong capping inversions. Satellite images show that topographically forced TLWs frequently occur around near-coastal offshore wind farms. Yet current understanding of how they interact with individual turbines and whole farm energy output is limited. This parametric study investigates the potential impact of TLWs on a UK near-coastal offshore wind farm, Westermost Rough (WMR) resulting from westerly – south-westerly flow over topography in the Southeast of England.

Computational fluid dynamics (CFD) modelling (using ANSYS-CFX) of TLW situations based on real atmospheric
15 conditions at WMR was used to better understand turbine level and whole wind farm performance in this parametric study based on real inflow conditions. These simulations indicated that TLWs have the potential to significantly alter the windspeeds experienced by and the resultant power output of individual turbines and the whole wind farm. The location of the wind farm in the TLW wave cycle was an important factor in determining the magnitude of TLW impacts, given the expected wavelength of the TLW. Where the TLW trough was coincident with the wind farm, the turbine windspeeds and power outputs were more
20 substantially reduced compared with when the TLW peak was coincident with the location of the wind farm. These reductions were mediated by turbine windspeeds and wake losses being superimposed on the TLW. However, the same initial flow conditions interacting with topography under different atmospheric stability settings produce differing near wind farm flow. Factors influencing the flow within the wind farm under the different stability conditions include differing: hill and coastal transition recovery, windfarm blockage effects and wake recovery. Determining how much of the differences in windspeed
25 and power output in the wind farm resulted from the TLW is an area for future development.

1   Introduction

Atmospheric Gravity Waves (AGWs) often result from displacement of flow by topographical obstacles in neutral or stable surface atmospheric conditions with a strong temperature inversion above the atmospheric boundary layer. They also form via jet stream turbulence, weather fronts, cold air outbreaks, thunderstorms, tornadoes, hurricanes, polar lows and other unknown
30 sources (Gossard and Hooke, 1975; Rasmussen and Aakjær, 1992; Romanova and Yakushkin, 1995; Chunchuzov et al., 2000;

Nappo, 2012). The flow displaced by these conditions oscillates to create waves which modulate the local wind speed. AGWs are frequent in the offshore environment and influence marine atmospheric boundary layer wind fields over large areas of the ocean, (e.g. Thomson et al., 1992; Vachon et al., 1994).

Strong stable capping temperature inversions aloft, often induced by changes in temperature at the coastal transition, provide a 'lid' to trap the waves created by topographical obstacles, resulting in horizontally propagating AGWs, known as Trapped Lee Waves (TLWs). In the last 12 years, AGW propagation instigated by windfarms themselves has been investigated (e.g. Smith, 2010; Allaerts and Meyers, 2017a, 2019, 2017b; Allaerts et al., 2018; Lanzilao and Meyers, 2020) and the impact of TLWs on onshore windfarms has recently been investigated (Xia et al., 2021; Draxl et al., 2021; Wilczak et al., 2019). However, to our knowledge, no one has investigated the influence of pre-existing TLWs on individual turbines or whole wind farms offshore and computational fluid dynamics (CFD) investigations of TLW-wind farm investigations have not been published. Considering their influence on offshore wind speeds, TLWs are likely to impact offshore wind power production. Thus, this research investigates the influence of TLWs on offshore wind farm power output using Unsteady Reynolds Averaged Navier Stokes (~~RANS~~URANS) CFD simulations. Although this work focuses on resolving standing waves, a URANS solver was preferred for reasons of numerical stability. Influences on the flow under differing stability conditions are summarised in Fig. 1.
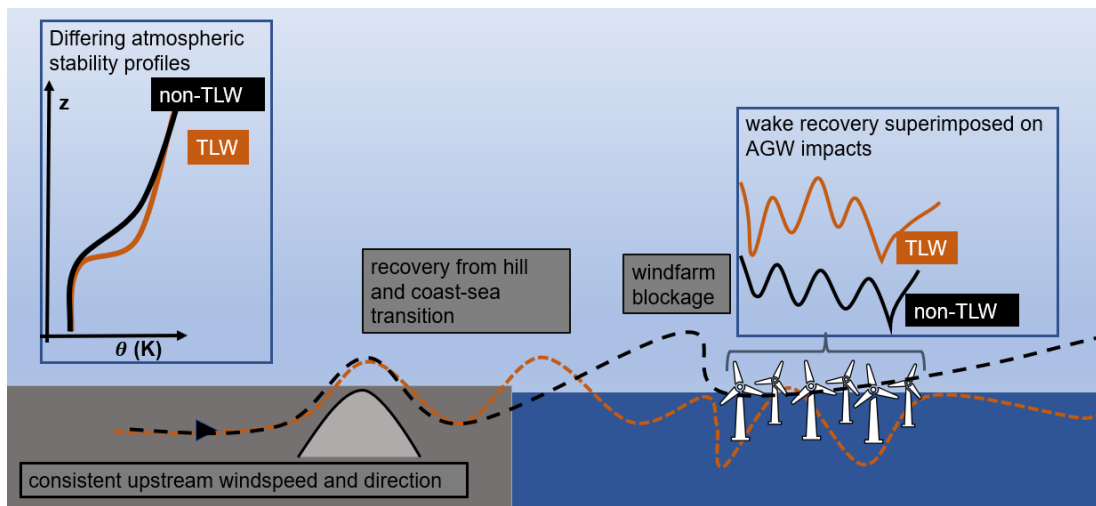
Figure 1. Interaction of consistent windspeed and direction with different stability conditions upstream of a topographical obstacle and an offshore wind farm. The dashed lines show the evolution of flow aligned with a single column of wind turbines. This flow evolves under different stability conditions, a strong capping inversion for the TLW (orange) and a conventionally neutral boundary layer (CNBL, black) without TLWs (non-TLW). Insets show stability profiles (left) and wind farm wake recovery superimposed on the background flow for a single column of turbines aligned with the prevailing wind direction.

We use a theoretical offshore wind farm downstream of a topographical obstacle to simulate the impact of TLWs on the wind power output. Although the set-up is theoretical, the layout used is based in the operational offshore wind farm at Westermost

Rough (WMR) off the East Yorkshire coast. This theoretical windfarm referred to as WMR throughout this paper. The following section covers identification of TLW conditions at WMR (section 2.1), sections 2.2 2.7 describe the modelling methodology in ANSYS CFX for TLWs at WMR. Section 3 presents and discusses the modelled impact of TLWs on the turbines and windfarm, the implications of TLWs on WMR are summarised in section 4 and suggested future investigations are included in section 5.

2   Methodology

2.1 TLW identification

SAR data from Sentinel 1a/b, pre-processed for 10m wind (DTU Wind Energy, 2021), were used to detect TLW events at Westermost Rough offshore windfarm (WMR, Fig. 2).
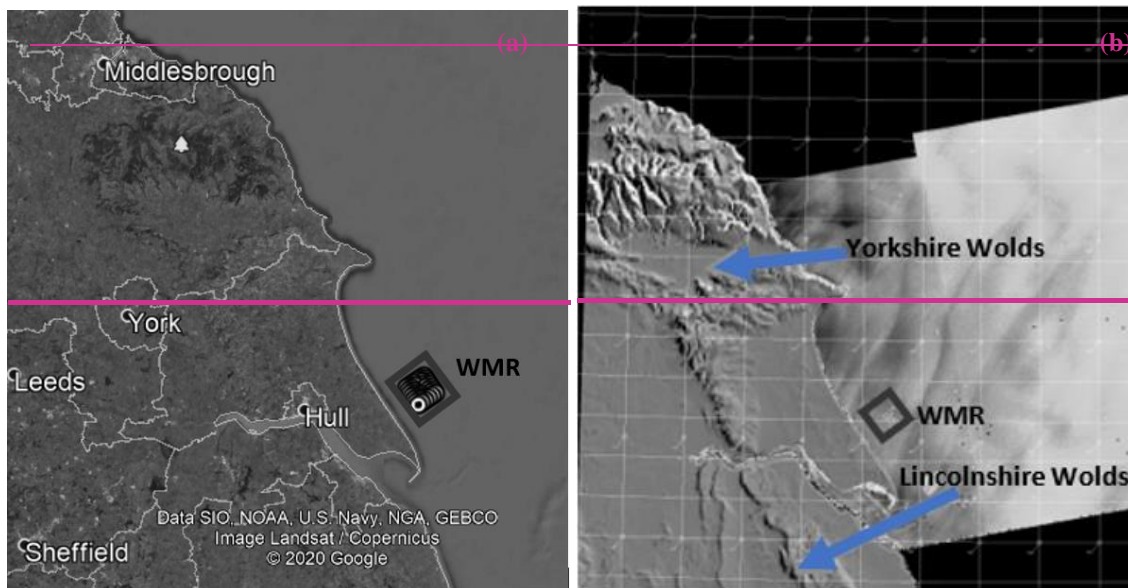

Figure 2.

1.1   Wave Damping

Erroneous wave reflection from the domain boundaries is a frequent problem in CFD models with AGWs. A solution to this problem is to introduce wave damping. Raleigh damping absorbs waves before they can be reflected at domain boundaries, it a) WMR location off the Holderness coast of North East England, WMR shown by grey polygon (Data SIO, NOAA, U.S. Navy, NGA, GEBCO, Image Landsat/Copernicus ©2020 @2021 Google).b) SAR image of WMR (DTU Wind Energy, 2016), raised topography shown by darker shades of grey, Location of WMR shown by grey polygon.

Sentinel 1a/b passed over WMR every 1-3 days in 2016 – 2017 around 06:15 or 17:45 UTC. The SAR images were visually inspected for TLWs in a similar manner to other studies (e.g. Li et al., 2013b; Li, 2004; Xu et al., 2016). TLW classification

3

of images was based on the appearance of a repeating linear pattern of fluctuating windspeeds, perpendicular to the prevailing wind direction at the location of WMR. A potential temperature vertical profile proxy for the site was taken from 97 vertical levels of ERA5 reanalysis data (ERA5, 2020) for the lowest 5 km of the atmosphere. The existence of a strong temperature inversion in ERA5 was used to confirm the likelihood of TLW formation. A TLW event at WMR was selected to provide the boundary conditions for CFD simulations and a CNBL event with a weak inversion, not strong enough to produce TLW, was selected as a control (Section 2.6).

2.2 Domain and Topography

For all RANS simulations, ANSYS CFX 18.0 was used with ANSYS Windmodeller as a front end to set up the simulations. The topography includes a simplified representation of a steep near-coastal ridge as in (Ollier et al., 2018), based on a two-dimensional hill profile. The hill dimensions are based on a 'Witch of Agnesi' profile (Fig. 3).
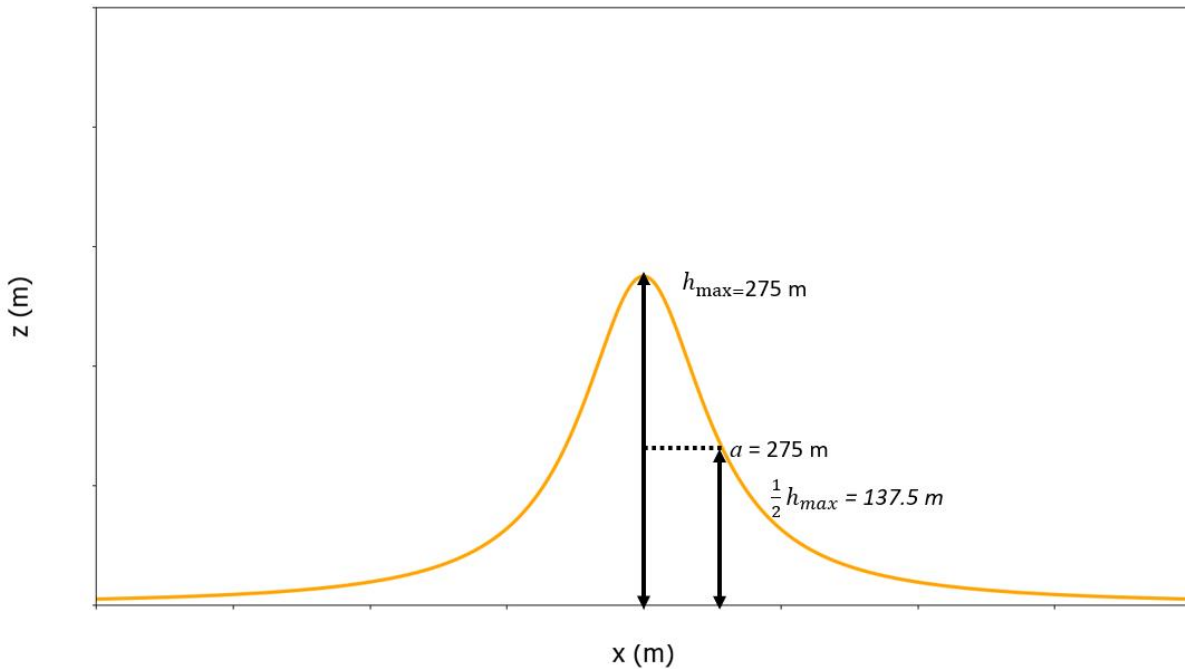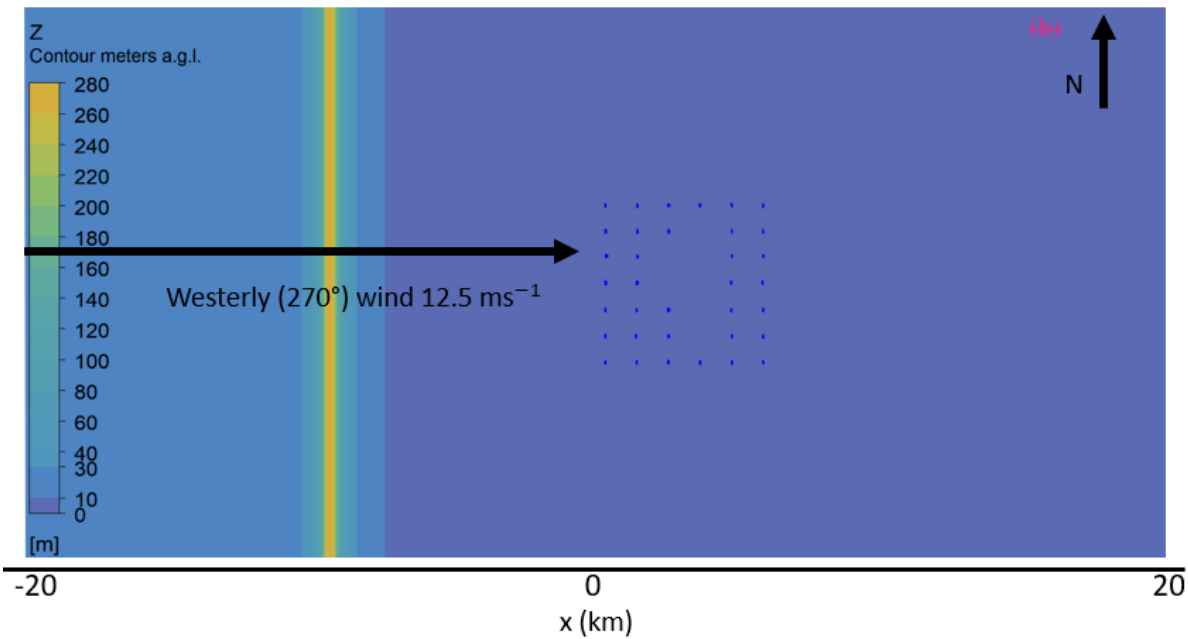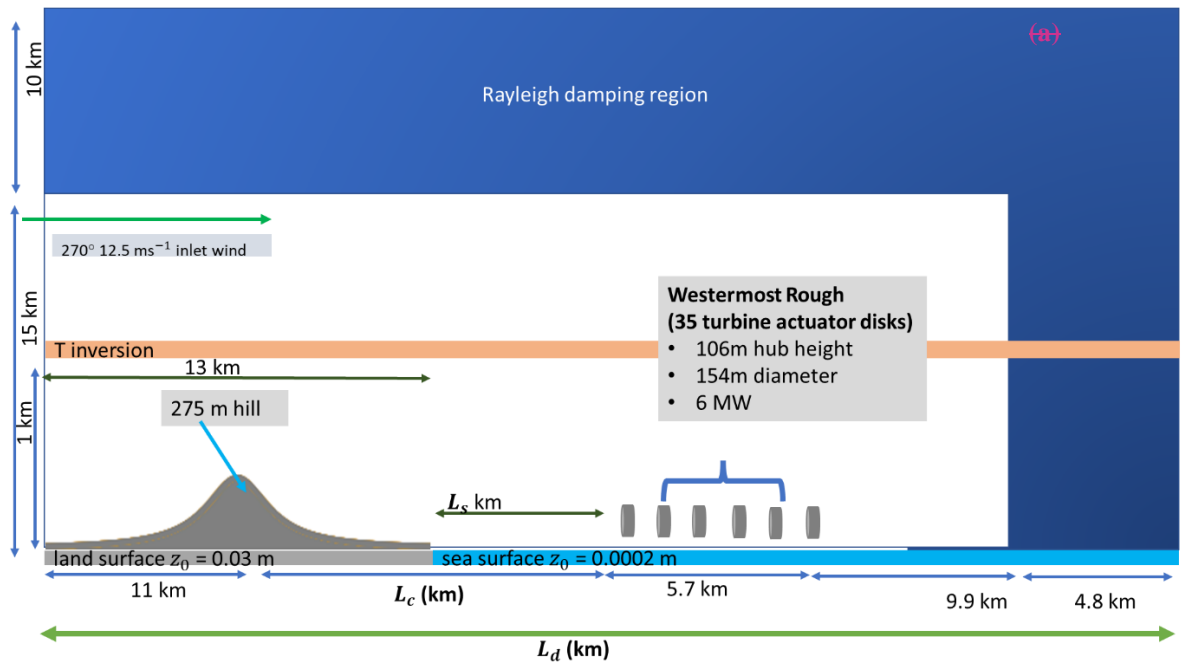

Figure 3. Witch of Agnesi shaped profile used in coastal ridge simulations (not to scale).

The hill height $h(x)$ depends on the maximum hill height h_{max}, (chosen as 275 m) and half width at half height a, (also chosen as 275 m) as a function of horizontal distance x from the centre of the hill (Eq. 1). This results in a very steep hill, with a slope ~ 65 % (~ 33°). N.B. Flow separation is expected at slopes ≥ 30 %.

$$h(x) = \frac{h_{max} \cdot a^2}{x^2 + a^2} \qquad\qquad 1$$

4

This is a very simplified hill compared to the actual topography upstream of WMR. Due to the complexity of the real terrain upstream of WMR, the simplified hill model does not attempt to capture the terrain features other than that of a simple hill, which is the same distance from the wind farm as WMR is from the coast with the aim of inducing TLWs.

This two-dimensional hill is elongated to form a ridge aligned perpendicular to the incoming westerly (270°) wind. The hilltop is 11 km from the inlet (Fig. 4a). There is flat coastal terrain at an elevation of 10 m above sea level (asl) upstream of the ridge, with a constant roughness length (z_0) of 0.03 m. The sea with constant roughness length (z_0 = 0.0002 m) is located downstream of the coastline as shown in (Fig. 4). All domains have an upper and outlet Rayleigh damping region (section 2.3).

95

6

To capture TLW peak interactions with WMR, a 41.4 km long domain was used (Fig. 4). This cuboid domain is 41.4 km long, 20 km wide and 25 km high (Fig. 4). These dimensions allow for insertion of topography and downstream actuator discs representing WMR. The flow reaches equilibrium before and after these obstacles before reaching the domain boundaries. Many studies use spanwise infinite wind farms, but as (Allaerts and Meyers, 2017a) notes, this exaggerates the blockage effect and the excitation of wind farm-produced TLWs, likely overestimating their strength. The present study allows for flow transport around the model of a finite wind farm. The height of the incompressible flow domain (25 km) was chosen to avoid non-physical numerical reflections of the gravity waves (section 2.3).

An extended domain of 46 km was used to assess the impact of TLWs hitting the wind farm at the trough of the TLW rather than the peak (Fig. 4). This domain follows the same layout as the 41.4 km domain but the distance between the hill and the wind farm was extended by 4.6km (Fig. 4), approximately half the TLW wavelength modelled in the 41.4 km domain simulations.

2.3 Wave Damping

Rayleigh damping at the domain boundaries was introduced to prevent unphysical wave reflections. Rayleigh damping, which absorbs waves before they can be reflected at domain boundaries, was first introduced in early, two-dimensional mountain wave models (Klemp and Lilly, 1978; Durran and Klemp, 1983) through the use of a simple damping term depending on the perturbation of a variable from its equilibrium value. In the current work, the Rayleigh damping, which absorbs waves before they can be reflected at domain boundaries, was first introduced in early, two-dimensional mountain wave models (Klemp and Lilly, 1978; Durran and Klemp, 1983) through the use of a simple damping term depending on the perturbation of a variable from its equilibrium value. This can be simplified to prognostic equation 1 (Warner, 2010). damping coefficient was split into two components, $\tau_z(z), \tau_x(x)$ (Eqs. 2-4) as a function of the x- and z- coordinates respectively, and damping (ξ_w) was added only to the right-hand side of the z-momentum equation using Eq. 5. This was done to provide damping layers at the top and outlet of the domain:

for $H_{max} \geq z \geq 0$: $\xi_\alpha = \tau(z)(\alpha - \overline{\alpha})$

$$ \tag{1} $$

$$ \tau_z(z) = \tau_{0z} \exp\left(-0.5\left(3.5 \frac{z - H_{max}}{z_\tau}\right)^2\right) \tag{2} $$

for $x < 0$:

$$ \tau_x(x) = 0 \tag{3} $$

for $x \geq 0$:

$$ \tau_x(x) = \tau_{0x} \exp\left(-0.5\left(3.5 \frac{x - r_\tau}{D_\tau}\right)^2\right) \tag{4} $$

for $H_{max} \geq z \geq 0$ and $x \geq 0$:

$$ \xi_w = (\tau_x(x) + \tau_z(z)) w \tag{5} $$

Where $\tau(z)$ is the Rayleigh damping coefficient and α is a dependent variable, with $\bar{\alpha}$ the mean value of the dependent variable. Damping terms ξ_u, ξ_w, ξ_θ were added to the right-hand side of the u, w, θ equations in early work (Klemp and Lilly, 1978; Durran and Klemp, 1983). These were set to gradually increase in the upper half of the domain. In a recent LES study (Allaerts and Meyers, 2017a) low wave reflection was also reported when there was space for at least one vertical wavelength, λ_z. The constants τ_{ux} and τ_{uz} (units of s⁻¹) are set equal to 1 kg m⁻³ s⁻¹/ρ_0, where ρ_0 is air density at sea level (1.23 kg m⁻³) resulting in a maximum damping at the domain top and outlet of 0.8 s⁻¹. x is the horizontal location in the domain (m) ($x = -20700, 20700$ for the 41.4 km domain, Fig. 4b), r_x is the distance from the centre of the domain where damping is implemented (20.7 km for the 41.4 km domain and 23 km for the 46 km domain), D_x is the characteristic horizontal length for which damping is applied (4.8 km, all domains e.g. Fig. 4a, H_{max} is the maximum domain height and z_x the characteristic vertical depth for which damping is applied. This latter value was chosen to correspond to 40% of the domain height, i.e., 10 km, in line with a recent LES study (Allaerts and Meyers, 2017a). In the same study, low wave reflection was also reported when there was space for at least one vertical wavelength, λ_z, beneath the damping layer (Allaerts and Meyers, 2017a), based on an earlier linear model (Klemp and Lilly, 1978), where λ_z is defined as:

$$\lambda_z = \frac{2\pi U}{N} \qquad \qquad \textbf{2}$$

where U is the bulk windspeed and N is the freestream Brunt-Väisälä frequency (Eq. 73).

$$N = \sqrt{\frac{g}{\theta}\frac{\partial \theta}{\partial z}} \qquad \qquad \textbf{3}$$

where g is gravitational acceleration in (ms⁻²), θ is potential temperature (K) and $\frac{\partial \theta}{\partial z}$ is the free atmosphere lapse rate.

In the current work the domain height is 3.2 λ_z.

Whilst damping layer strength, depth, location and how the damping layers are implemented varies between studies, so do the atmospheric conditions (windspeed and inversion strength), domain dimensions, grid resolution, topography, wind farms sizes and layouts. Thus, it is not possible to directly compare the methodologies and deduce the optimal conditions to transfer to other studies. Recent studies (Ollier et al., 2018; Jia et al., 2019) used RANS to model TLWs, but do not detail their damping methodology. The literature discussed here uses LES configurations rather than RANS, some of which include a precursor domain (Gadde and Stevens, 2019; Wu and Porté-Agel, 2017), unlike the current work. Domain top Rayleigh damping strength ranged from 0.0001s⁻¹ – 0.016s⁻¹ in (Allaerts and Meyers, 2017a; Gadde and Stevens, 2019; Haupt et al., 2019; Hills and Durran, 2012)(Allaerts and Meyers, 2017a; Gadde and Stevens, 2019; Haupt et al., 2019; Hills and Durran, 2012) with a range of upper level damping thicknesses (1–16 km). A three-dimensional mountain ridge was included in (Hills and Durran, 2012), and no wind farm was included. A damping layer of 16 km in the vertical, from z = 20 km to the domain extent (z = 36 km)

was used in a very large domain (1200 km x 1200 km x 36 km), no inflow or outflow damping was included. TLW reflection was observed with stronger domain top damping in (Hills and Durran, 2012). The maximum damping in this layer was 0.005 s^{-1}, gradually increasing from 0 s^{-1} outside the layer.

160   Damping near domain inlet/outlet boundaries is not consistent in all studies; some use an outflow damping, some do not; and some have inflow and outflow damping. In two-dimensional models containing a simple hill and no turbines ~~(Haupt et al., 2019)~~(Haupt et al., 2019), inflow and outflow damping layers were not important for the solution in very long domains (200 km). However, upper-level damping was essential for the same domains, with optimal damping of 0.005 s^{-1}. Further, outflow damping reduced spurious upstream waves in shorter domains, but did not eliminate them. With shorter upstream distance,

165   with damping at the inflow, outflow and upper level, an LES model showed reasonable agreement with an analytical solution ~~(Haupt et al., 2019)~~(Haupt et al., 2019). Unfortunately, the domain dimensions were not included to contextualise these findings. Quasi-stationary topographic TLWs were modelled in a relatively shallow LES domain (22 km x 19 km x ~3 km) with 3 km high complex mountain terrain (Li et al., 2013a). Interestingly, no problems with wave reflection were reported, and damping was not discussed.
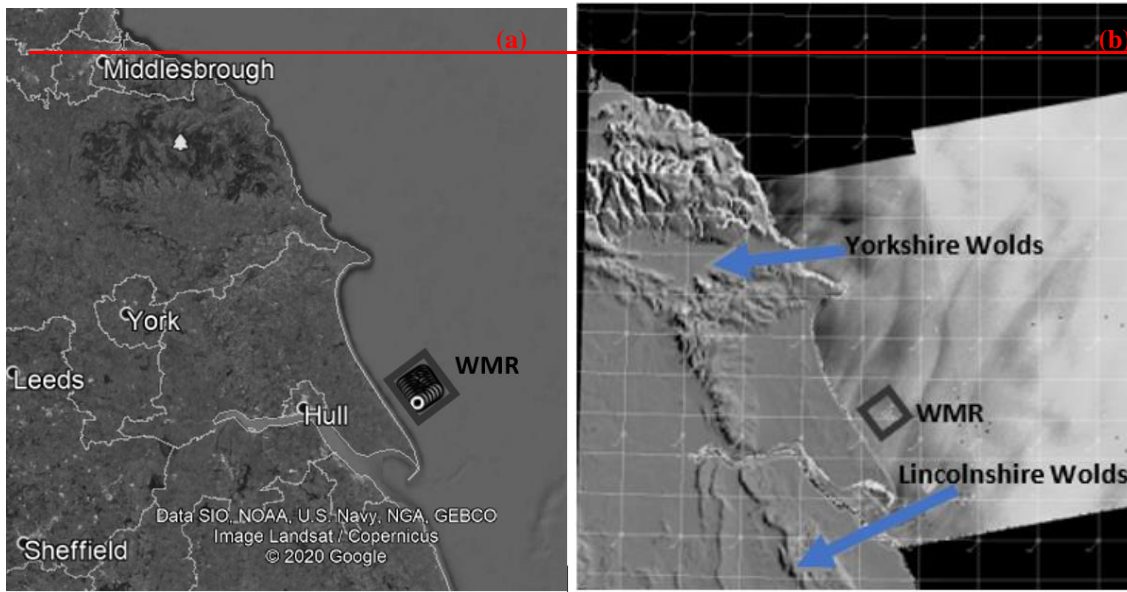
170   Notable wind farm LES studies with wind farm induced TLWs include (Allaerts and Meyers, 2017a; Maas and Raasch, 2022; Wu and Porté-Agel, 2017; Smith, 2010). The study in (Allaerts and Meyers, 2017a) used 10km upper-level damping (0.0001 s^{-1}) and 4.8km outflow damping (0.03 s^{-1}) applied with a gradually increasing cosine profile within a 38.4 x 4.8 x 25 km domain. The domain contained a spanwise infinite wind farm (180 regularly spaced turbines) over a sea surface of constant z_0, 0.0002m.

175   The following section covers identification of TLW conditions at WMR (section 2.1), sections 2.2-2.7 describe the modelling methodology in ANSYS CFX for TLWs at WMR. Section 3 presents and discusses the modelled impact of TLWs on the turbines and windfarm, the implications of TLWs on WMR are summarised in section 4 and suggested future investigations are included in section 5.

2   Methodology

2.1 TLW identification

180   SAR data from Sentinel 1a/b, pre-processed for 10m wind (DTU Wind Energy, 2021), were used to detect TLW events at Westermost Rough offshore windfarm (WMR, Fig. 2).
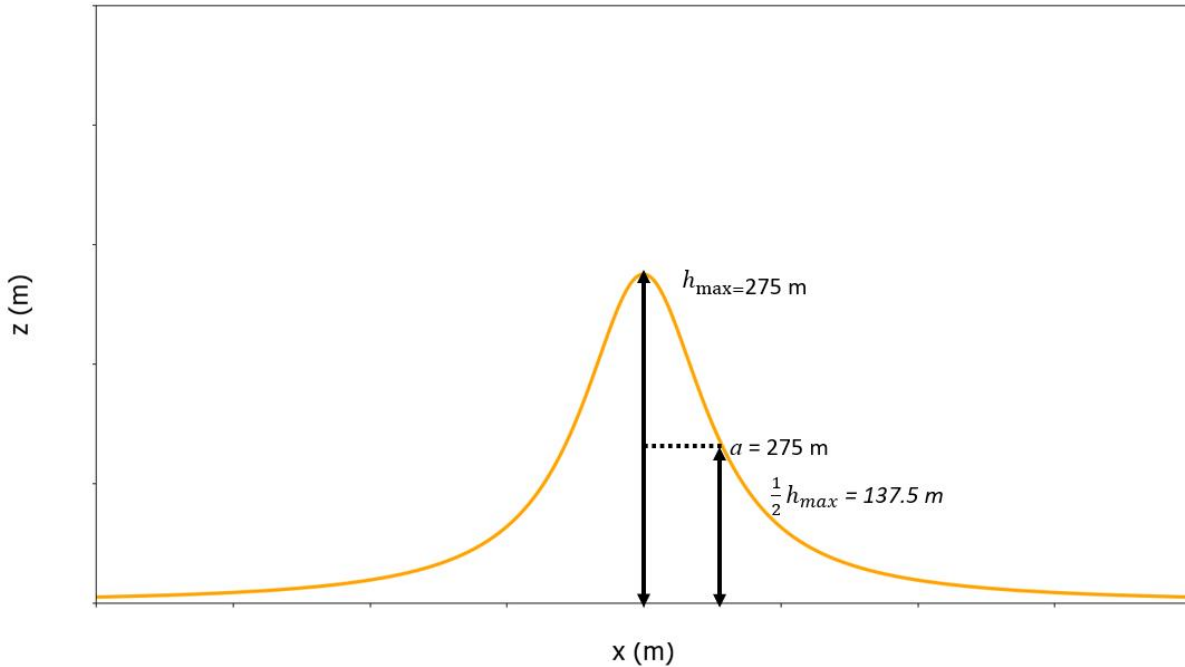
Figure 2. a): WMR location off the Holderness coast of North East England, WMR shown by grey polygon (Data SIO, NOAA, U.S. Navy, NGA, GEBCO, Image Landsat/Copernicus ©2020 @2021 Google).b) SAR image of WMR (ENVISAT and Sentinel 1 surface wind field processing), raised topography shown by darker shades of grey, Location of WMR shown by grey polygon.

Sentinel 1a/b passed over WMR every 1-3 days in 2016 – 2017 around 06:15 or 17:45 UTC. The SAR images were visually inspected for TLWs in a similar manner to other studies (e.g. Li et al., 2013b; Li, 2004; Xu et al., 2016). TLW classification of images was based on the appearance of a repeating linear pattern of fluctuating windspeeds, perpendicular to the prevailing wind direction at the location of WMR. A potential temperature vertical profile proxy for the site was taken from 97 vertical levels of ERA5 reanalysis data (ERA5, 2020) for the lowest 5 km of the atmosphere. The existence of a strong temperature inversion in ERA5 was used to confirm the likelihood of TLW formation. A TLW event at WMR was selected to provide the boundary conditions for CFD simulations and a CNBL event with a weak inversion, not strong enough to produce TLW, was selected as a control (Section 2.6).

2.2 Domain and Topography

For all RANS simulations, ANSYS-CFX 18.0 was used with ANSYS Windmodeller as a front end to set up the simulations. The topography includes a simplified representation of a steep near coastal ridge as in (Ollier et al., 2018), based on a two-dimensional hill profile. The hill dimensions are based on a 'Witch of Agnesi' profile (Fig. 3).
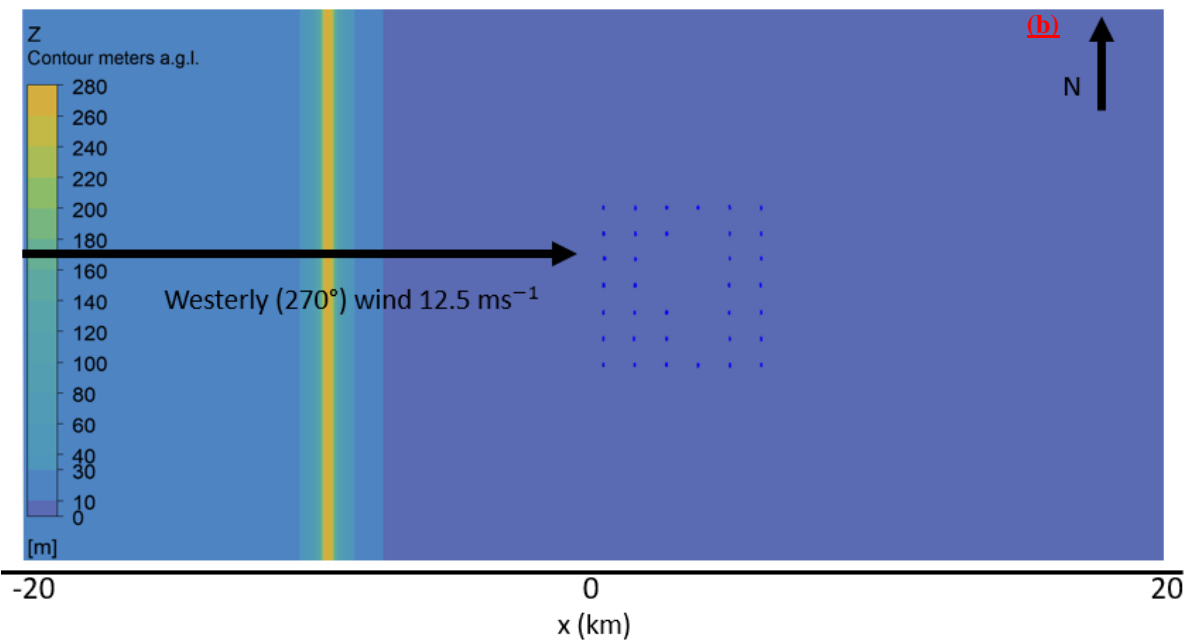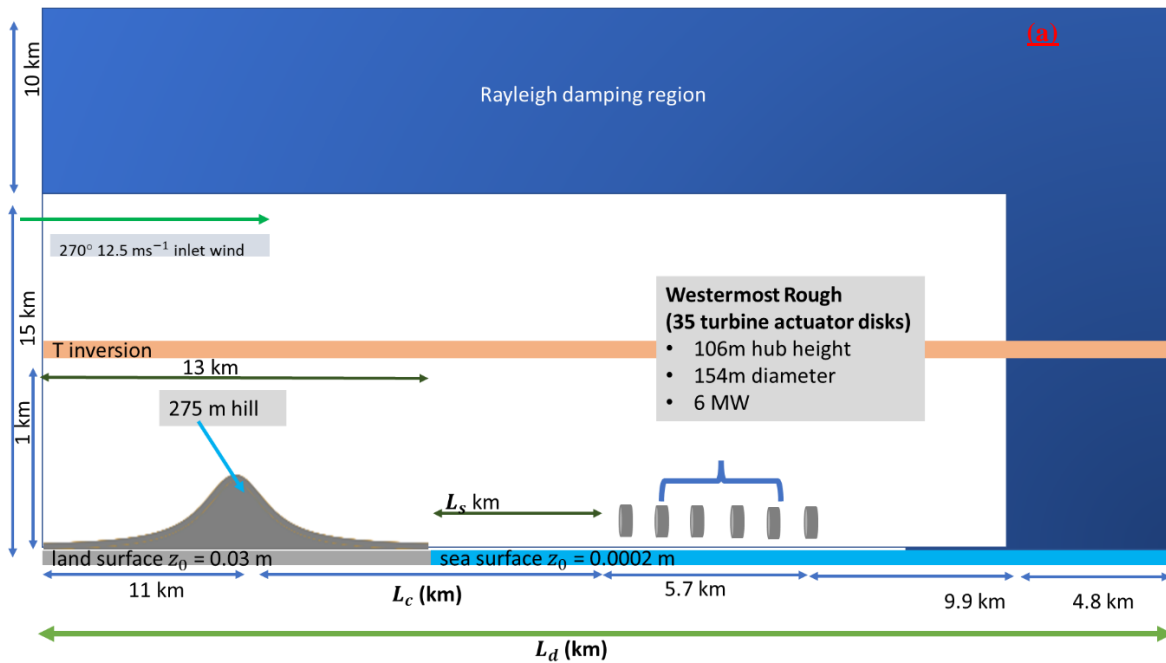
200 **Figure 3. Witch of Agnesi shaped profile used in coastal ridge simulations (not to scale).**

The hill height $h(x)$ depends on the maximum hill height h_{max}, (chosen as 275 m) and half-width at half-height a, (also chosen as 275 m) as a function of horizontal distance x from the centre of the hill (Eq 4). This results in a very steep hill, with a slope ~ 65 % (~33°). N.B. Flow separation is expected at slopes $\geq$ 30 %.

$$h(x) = \frac{h_{max}.a^2}{x^2 + a^2}$$

4

This is a very simplified hill compared to the actual topography upstream of WMR. Due to the complexity of the real terrain

205 upstream of WMR, the simplified hill model does not attempt to capture the terrain features other than that of a simple hill, which is the same distance from the wind farm as WMR is from the coast with the aim of inducing TLWs.

This two-dimensional hill is elongated to form a ridge aligned perpendicular to the incoming westerly (270°) wind. The hilltop is 11 km from the inlet (Fig. 4a). There is flat coastal terrain at an elevation of 10 m above sea level (asl) upstream of the ridge, with a constant roughness length (z_0) of 0.03 m. The sea with constant roughness length (z_0 = 0.0002 m) is located

210 downstream of the coastline as shown in (Fig. 4). All domains have an upper and outlet Rayleigh damping region (section 2.3).

Figure 4. a) Diagram of the WM simulation domain (not to scale) for the coastal hill cases at WMR. For the 41.4 km domain L_s, L_c and L_d are 8 km, 10 km and 41.4 km, respectively. For the 46 km domain L_s, L_c and L_d are 12.5 km, 14.6 km and 46 km, respectively (not to scale). b) view from WM domain for WMR coastal hill case, see legend for heights (m). Each yellow dot represents a single turbine location (axes is not to scale).

To capture TLW peak interactions with WMR, a 41.4 km long domain was used (Fig. 4). This cuboid domain is 41.4 km long, 20 km wide and 25 km high (Fig. 4). These dimensions allow for insertion of topography and downstream actuator discs representing WMR. The flow reaches equilibrium before and after these obstacles before reaching the domain boundaries. Many studies use spanwise infinite wind farms, but as (Allaerts and Meyers, 2017a) notes, this exaggerates the blockage effect and the excitation of wind farm produced TLWs, likely overestimating their strength. The present study allows for flow transport around the model of a finite wind farm. The height of the incompressible flow domain (25 km) was chosen to avoid non-physical numerical reflections of the gravity waves (section 2.3).

An extended domain of 46 km was used to assess the impact of TLWs hitting the wind farm at the trough of the TLW rather than the peak (Fig. 4). This domain follows the same layout as the 41.4 km domain but the distance between the hill and the wind farm was extended by 4.6km (Fig. 4), approximately half the TLW wavelength modelled in the 41.4 km domain simulations.

2.3 Wave Damping

In the current work the domain height is $3.2\ \lambda_z$.

Rayleigh damping at the domain boundaries was introduced to prevent unphysical wave reflections. The damping coefficient was split into two components, $\tau_z(z), \tau_x(x)$ (Eqs. 5-7) as a function of the x and z coordinates respectively, and damping (ξ_w) was added only to the right-hand side of the z-momentum equation using Eq. 8. This was done to provide damping layers at the top and outlet of the domain:

for $H_{max} \geq z \geq 0$:

$$\tau_z(z) = \tau_{0z}\ \exp\left(-0.5\left(3.5\ \frac{z - H_{max}}{z_\tau}\right)^2\right)$$ 5

for $x < 0$:

$$\tau_x(x) = 0$$ 6

for $x \geq 0$:

$$\tau_x(x) = \tau_{0x}\ \exp\left(-0.5\left(3.5\ \frac{x - r_\tau}{D_\tau}\right)^2\right)$$ 7

for $H_{max} \geq z \geq 0$ and $x \geq 0$:

$$\xi_w = (\tau_x(x) + \tau_z(z))\ w$$ 8

The constants τ_{0x} and τ_{0z} (units of s^{-1}) are set equal to 1 kg m^{-3} s^{-1}/ρ_0, where ρ_0 is air density at sea level (1.23 kg m^{-3}) resulting in a maximum damping at the domain top and outlet of 0.8 s^{-1}. x is the horizontal location in the domain (m) (x = -20700, 20700 for the 41.4 km domain, Fig. 4b), r_τ is the distance from the centre of the domain where damping is implemented (20.7 km for the 41.4 km domain and 23 km for the 46 km domain), D_τ is the characteristic horizontal length for which damping is

13

240 applied (4.8 km, all domains e.g. Fig. 4a, H_{max} is the maximum domain height and z_τ the characteristic vertical depth for which damping is applied. This latter value was chosen to correspond to 40% of the domain height, i.e., 10 km, in line with a recent LES study (Allaerts and Meyers, 2017a).

In the absence of consistent guidance in the literature regarding the optimal set up of Rayleigh damping layers, the best configuration, used for all the domains in this chapter, was based on modification of the default Rayleigh damping in ANSYS

245 Windmodeller. The damping strength was unchanged but the location and thickness of the damping layers were modified. This was determined by trial and error. Key findings during this process were that increased domain length and depth with outflow and upper-level damping resolved most wave reflection. We did not find inflow damping helpful and the damping layers thinner than those used were insufficient. However, these settings are specific to the dimensions, contents and atmospheric conditions of the domain used in this research. Whilst the damping layer strength used in this research is higher than in previous

250 studies, Durran and Klemp (1983)(1983) found that the depth of the damping layer more important and damping strength did not strongly influence the solution.

2.4 Boundary conditions

At the inlet (Western plane), Dirichlet boundary conditions (i.e., prescribed profiles) were applied for the velocity vector, the

255 potential temperature θ and the turbulence quantities (turbulence kinetic energy k and turbulence dissipation rate ε). For the pressure, a zero-gradient condition is applied. The inlet profiles for the relevant variables were set up as follows: below the boundary layer height, h_{BL}, the velocity profile follows a log profile, while above it, the profile is set to the velocity value at the top of the boundary layer, V_G. With the flow directed along the x axis, velocity profiles (Eq. 9-10) were used for the velocity components (V_x, V_y, V_z):

$$V_x(z) = min\left(\frac{u_*}{\kappa}\ln\left(\frac{z}{z_{0,us}}\right), V_G\right) \qquad \textbf{9}$$

$$V_y = V_z = 0 \qquad \textbf{10}$$

260 Where $z_{0,us}$ is the surface roughness upstream. The von Kármán constant, κ is set to a value of 0.41. The roughness length z_0 is used to set the profile by calculating the friction velocity (u_*, Eq. 11). The boundary layer height is calculated from the empirical relationship in Eq. 11 (Garratt, 1994)(Garratt, 1994).

$$h_{BL} = 0.25\frac{u_*}{f} \qquad \textbf{11}$$

265 With f is the Coriolis parameter (1.2 x 10^{-4} s^{-1}). The inlet profiles for the turbulence kinetic energy and dissipation rate are defined in Eq. s 12-14:

14

$$k(z) = max\left[\frac{u_*^2}{\sqrt{C_\mu}}\left(1 - \frac{z}{h_{BL}}\right)^{1.68}, 10^{-4}\ m^2/s^2\right]$$

12

13

$$\varepsilon(z) = max\left[\frac{u_*^3}{\kappa z} 1.03\ F_{cor}\ exp\left(-2.8\left(\frac{z}{h_{BL}}\right)^2\right), 10^{-4}\ m^2/s^3\right]$$

14

$$F_{cor} = \left[1 + \frac{0.015}{z^{0.9}} max\left(0, ln\frac{z}{z_0}\right)\right]$$

where F_{cor} is a roughness dependent correction factor. The profiles for the turbulence quantities in Eq. s 12-14 are approximate fits to numerical results obtained for a one-dimensional simulation of a developing boundary layer over the sea, after 24 hours of physical time (Montavon et al., 2012).

At the outlet (Eastern plane) and at the top of the domain, an entrainment opening boundary condition is used which applies: zero-gradient condition on the velocity, zero-gradient on the potential temperature and turbulence quantities when the flow is locally out of the domain. If the flow is entering the domain at those locations, the model then applies the same prescribed profiles as those used for the inflow. A Dirichlet boundary condition for the pressure, where the prescribed pressure profile is calculated to satisfy the hydrostatic balance associated with the potential temperature profile applied at the inflow[1]. At the sides of the domain (Northern and Southern planes), symmetry conditions are used for all variables. At the ground, no-slip boundary conditions are used for the velocity, using wall functions to characterise the momentum fluxes as a function of the local roughness length and friction velocity u_* (ms^{-1}, Eq. 15) (ANSYS, 2017):

$$u_* = C_\mu^{1/4} k^{1/2}$$

15

where C_μ is the turbulence model constant (0.09).

For neutral surface layer simulations (section 2.6), adiabatic (i.e., zero heat flux) conditions are used for the potential temperature and for the turbulence kinetic energy. Where surface stability is included, diabatic (heat flux) conditions are used for potential temperature and for the turbulence kinetic energy.

All simulations use a 270° 12.5 ms^{-1} reference wind speed at the turbine hub height (106 m). The closure for the turbulence dissipation rate at the ground is provided by ε, (Eq. 13). Atmospheric stability conditions are detailed in section 2.5. The Coriolis force has been shown to deflect wakes in wind farms and wake deflection is more pronounced in stable boundary

---

[1] When no flow prevails in the domain, the momentum conservation equation in the vertical is simplified to $\frac{\partial p}{\partial z} = g\rho\frac{1}{\theta_0}(\theta - \theta_0)$. The pressure profile used at the outflow is calculated by integrating this relationship from the ground to the top of the domain, using the prescribed profile for θ_{in} at the inflow, and the reference potential temperature θ_0. When using a pressure profile not satisfying the hydrostatic balance, the model generates flow acceleration or slow-down that can destabilise the solution. .

layers (e.g. Gadde and Stevens, 2019). However, to isolate the effects of stability and the Coriolis effect, the Coriolis force is 'switched off' for all simulations.

This model assumes isotropic turbulent viscosity where the ratio of Reynolds stress and rate of deformation is equal in all directions. Whilst the k-ε RANS model is less accurate in the near wake region (e.g. Argyle, 2014), for the whole farm simulations in this research the far wake is more important. The k-ε turbulence model uses modified C_μ (0.03, Eq. 15) (Montavon et al., 2011) for all simulations as it performed best in preliminary trials, increasing the eddy viscosity in turbine wakes and reducing numerical noise in TLW simulations.

2.5 Atmospheric conditions

For the simulations including atmospheric stability , the freestream potential temperature gradient, was set to 3.3 x 10^{-3} K km^{-1} in line with the International Standard Atmosphere (ISO 2533:1975). The potential temperature profile is set as follows:

for $z < z_{inv} - d$:

$$\theta_{in} = \theta_1 \qquad\qquad 16$$

for $z_{inv} - d < z < z_{inv}$:

$$\theta_{in} = \theta_1 + (\partial\theta/\partial z)_{inv}[z - (z_{inv} - d)] \qquad\qquad 17$$

$$(\partial\theta/\partial z)_{inv} = (\theta_0 + (\partial\theta/\partial z)_0 . z_{inv} - \theta_1)/d \qquad\qquad 18$$

for $z > z_{inv}$:

$$\theta_{in} = \theta_0 + (\partial\theta/\partial z)_0 z \qquad\qquad 19$$

where z is height, z_{inv} is height of the top of the inversion layer, $d = z_{inv} - dz_{inv}$ is the inversion layer depth and dz_{inv} the inversion base. $(\partial\theta/\partial z)_{inv}$ is the lapse rate for the temperature inversion and $(\partial\theta/\partial z)_0$ is the free atmosphere lapse rate (Montavon, 2017; Ollier et al., 2018), θ_{in} is the potential temperature at the inflow, θ_0, the reference potential temperature and θ_1, potential temperature for z at the inflow.

Neutral atmospheric stability was used as a control for the 41.4 km and 46 km domains. In these cases, the atmospheric stability conditions were neutral throughout, with a constant potential temperature of 288 K (Ollier et al., 2018), (purple dots, Fig. 6). These simulations were given the short code '0N' (Table 1, Table 2). TLW simulations included a capping inversion with lapse rate $(\partial\theta/\partial z)_{inv} = 7.6$ K km^{-1} and a stable surface layer (short code '7S', e.g. r7Sh-WMR, Table 1, Table 2, the temperature profile was based on the atmospheric conditions during a TLW event at WMR (Fig. 5a, Fig. 6Fig. 5).). In the ERA5 data, there was a temperature inversion around 1km – 2.5km with $(\partial\theta/\partial z)_{inv} = 7.8$ K km^{-1} (blue crosses, Fig. 6). This ERA5 profile also had a stable surface layer with an approximately -2 K surface offset, increasing to near neutral at z ~300 m.

A -2K surface temperature offset was applied in the 7S simulations gradually increasing to neutral at z ~30 m at the inlet. As the profile develops in the domain this vertical distance increases to 300 m, comparable to the ERA5 stable surface depth. The temperature inversion was introduced using Eq. s 16-19, (Fig. 5, (Montavon, 2017; Ollier et al., 2018)) with the following parameters: z_{inv}= 2.5km, $z_{inv} - d$ = 1km, $(\partial\theta/\partial z)_{inv}$ = 7.6 K km^{-1} (Fig. 5, Fig. 6) at the surface. This is the basis for proxy atmospheric conditions for TLW formation, conditioned on the potential temperature profile, wind direction and windspeed at a reference height 106 m (turbine hub height). To assess the impact of the stable surface layer, the same temperature inversion with a neutral surface layer was included (green dash line Fig. 6, r7Nh-WMR, Table 1, Table 2).
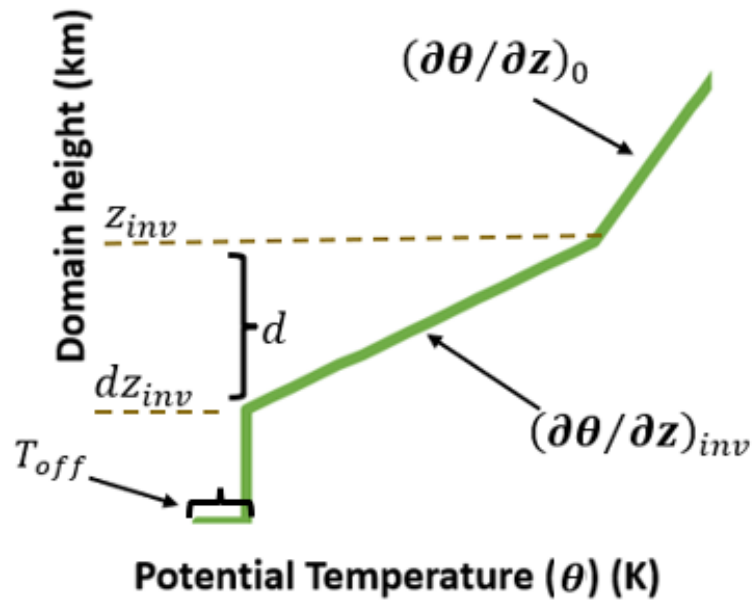
Figure 5. Potential temperature schematic used in the simulations with stability where z is height, z_{inv} is height of the top of the inversion layer, d is the distance between the top and bottom of the inversion layer. $(\partial\theta/\partial z)_{inv}$ is the lapse rate for the temperature inversion and $(\partial\theta/\partial z)_0$ is the lapse rate above the inversion and T_{off} is the surface temperature offset.

For a control simulation based on real atmospheric conditions at WMR, the weak CNBL simplified profile (gold dashes, Fig. 6) was used. This is based on the weak CNBL event identified in SAR (Fig. 7b). The ERA5 data (blue crosses, Fig. 6) was taken from the same location as the capping inversion TLW case. The inversion base is at 0.6 km, with a 3.3 K km^{-1} lapse rate. As $\left(\partial\theta/\partial z_{inv}\right)$ = 3.3 K km^{-1} is the same as the freestream potential temperature gradient $\left(\partial\theta/\partial z_0\right)$, there is not an upper limit to the inversion. These simulations were given the short code '3N' (Table 1).
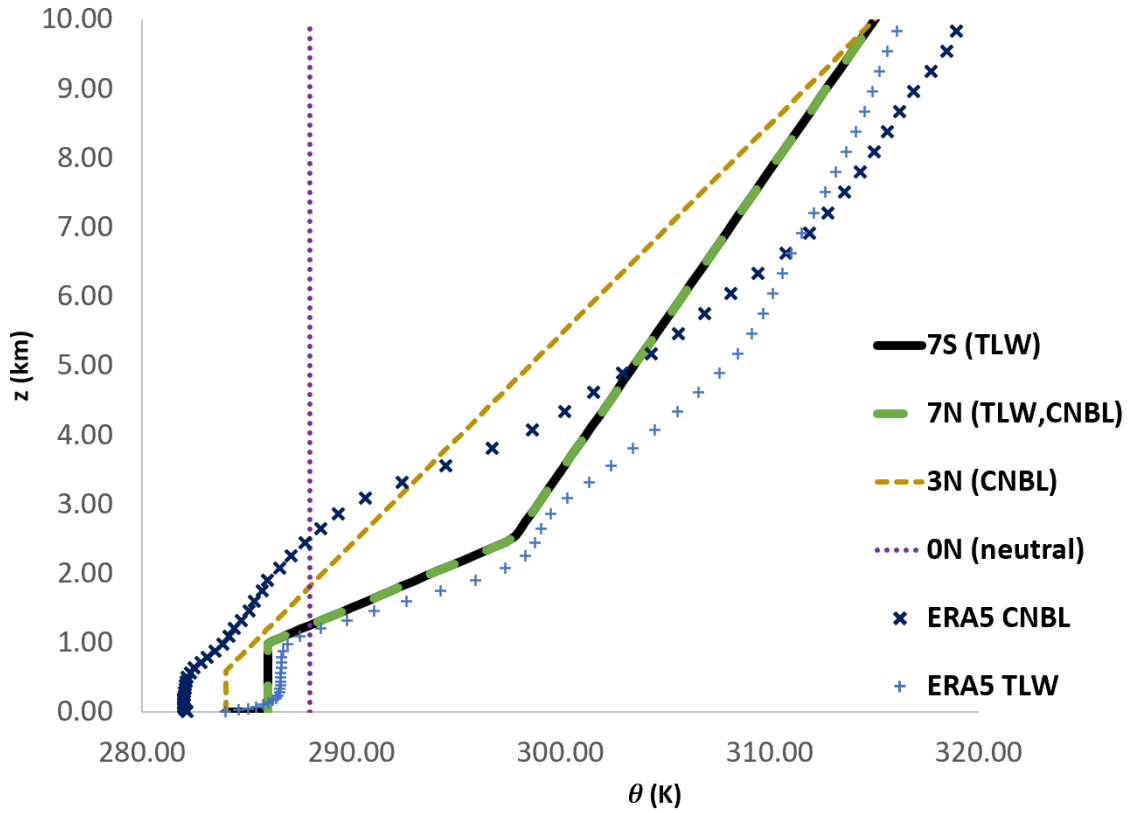
Figure 6. Stability profiles from ERA5 non-TLW (CNBL) (blue cross) and TLW events (blue diamond) and WM inflow conditions approximating to the same events. Where 7S is $(\partial\theta/\partial z)_{inv}$ = 7.6 K km^{-1} with stable surface layer, 7N is $(\partial\theta/\partial z)_{inv}$ = 7.6 K km^{-1} with neutral surface layer. 3N is $(\partial\theta/\partial z)_{inv}$ = 3.3 K km^{-1} with neutral surface layer and 0N is neutral throughout. Short codes summarised in Table 1.
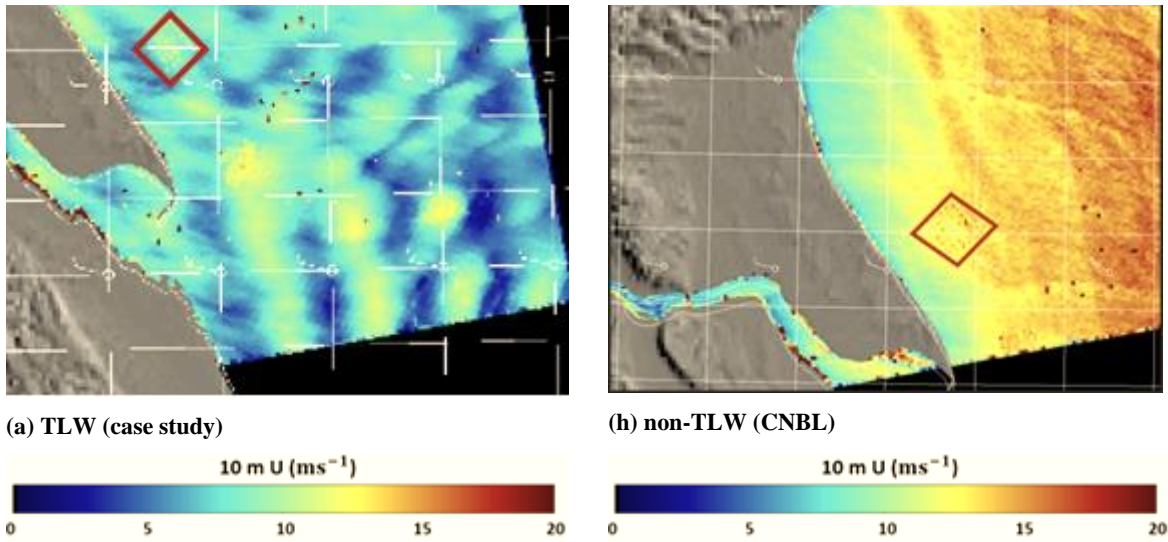
(a) TLW (case study)

(h) non-TLW (CNBL)

Figure 7. Examples of TLWs and non-TLW events detected in SAR images at WMR. Red polygon shows location of WMR. Legend shows 10 m windspeeds (ms⁻¹). Images adapted from (DTU Wind Energy, 2021, 2016; ENVISAT and Sentinel 1 surface wind field processing)**.**

Table 1. Short codes for simulations

Short code	definition
domain length	
r	Regular domain (41.4 km)
x	Extended domain (46 km)
Capping inversion	$\partial\theta/\partial z_{inv}$ (K km⁻¹), dz_{inv} (km), z_{inv} (km)
7	7.6, 2.5, 1.5
3	3.3, 25 (domain extent), 0.6
0	No inversion, neutral conditions throughout
Surface stability	
S	Stable surface layer
N	Neutral surface layer (CNBL)
Topography	
h	Coastal hill
Wind farm	
WMR	WMR wind farm
NWF	No wind farm

19

Table 2. Overview of simulations

Simulation	Inlet U (ms^{-1})	Stability $\partial\theta/\partial z_{inv}$ (K km^{-1})	z_{inv} (km)	d (km)	Surface stability	dz_{inv} (km)	turbines (number, layout)	topography	dimensions x,y,z (km)
r7Sh-WMR (TLW peak)	12.5	7.6	2.5	1	stable -2 K	1.5	35 WMR layout	coastal hill, ocean	41.4 x 20 x 25
r7Sh-NWF	12.5	7.6	2.5	1	stable -2 K	1.5	-	coastal hill, ocean	41.4 x 20 x 25
r7Nh-WMR	12.5	7.6	2.5	1	neutral	1.5	35 WMR layout	coastal hill, ocean	41.4 x 20 x 25
r3Nh-WMR	12.5	3.3	25	3	neutral	0.6	35 WMR layout	coastal hill, ocean	41.4 x 20 x 25
r0Nh-WMR	12.5	-	-	-	neutral	-	35 WMR layout	coastal hill, ocean	41.4 x 20 x 25
x7Sh-NWF	12.5	7.6	2.5	1	stable -2 K	1.5	-	coastal hill, ocean	46 x 20 x 25
x7Sh-WMR (TLW trough)	12.5	7.6	2.5	1	stable -2 K	1.5	35 WMR layout	coastal hill, ocean	46 x 20 x 25

2.6 Turbine set up

345 The WMR layout and spacing was used for all simulations (Fig. 8). The WMR layout was rotated by 33° to align with the 270° inlet wind in the domain (Fig. 4, Fig. 8~~).~~). This alignment is equivalent to south westerly winds reaching WMR at turbine row A.
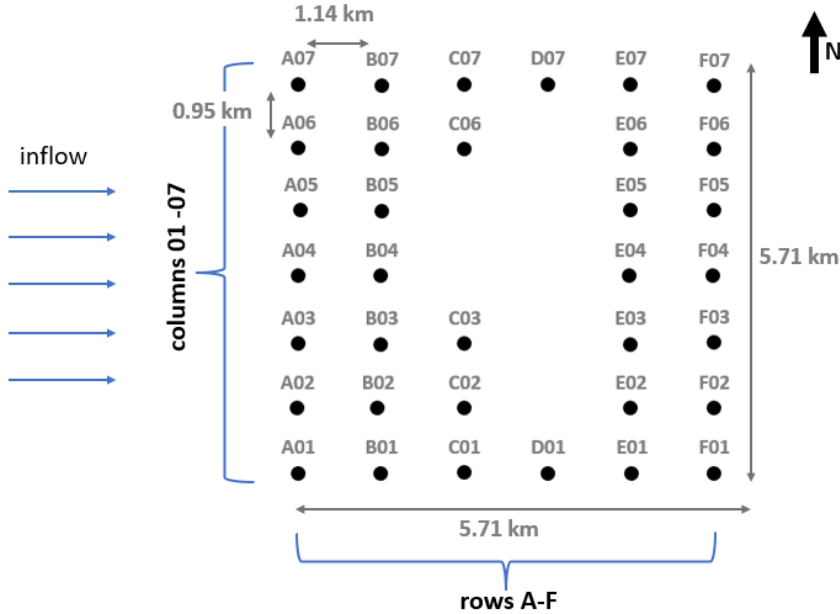
Figure 8. WMR layout for WM domain, using the same spacing as WMR but rotated 30° to align with the 270 degree wind direction 350 in the domain (the equivalent of SW flow reaching WMR). Rows and columns labelled as referred to in the text.

Turbines were modelled as actuator discs (ADs) whose thrust is conditioned on the upstream wind speed and the thrust curve is modified to be a function of disc (as opposed to freestream) wind speed. The actual hub heights (106 m), spacing (0.95 within row, 1.14 km between rows) and rotor diameters (154 m) of WMR turbines were used in this model (Fig. 8), with AD 355 thickness ~38.5 m. All turbines were set to be operational during the simulations and to yaw to the local flow direction (Ollier et al., 2018). A 6MW, 154m diameter turbine theoretical power curve was used with thrust data for a Siemens 3.6 MW direct drive wind turbine (SWT-3.6-107) (Appendix A). For individual turbines, local turbulence intensity is determined by Eq. 20. The freestream turbulence intensity offshore was 0.07 for all simulations.

$$TI = \frac{\sqrt{\frac{2}{3}k}}{U_{hub}}$$

20

Where k is turbulent kinetic energy, U_{hub} is the windspeed at the turbine hub.

360

Turbine U_{us} is obtained by using Actuator Disc theory to convert U_{hub} (Eq. 2120) to U_{us}.

$$U_{hub} = U_\infty(1 - a_i) \qquad \textbf{21}$$

where:

$$a_i = \frac{1}{2}(1 - \sqrt{1 - C_T(U_\infty)}) \qquad \textbf{22}$$

Where U_{hub} is the windspeed at the turbine rotor, C_T is the thrust coefficient, U_∞ is the freestream windspeed and a_i is the axial induction factor.

365 Turbine meshing was set up as in Ollier et al., (2018). The background horizontal resolution (outside of the rotor regions) for the model domain is 60 m (Appendix B). 150 vertical levels were used, and the first cell above ground is 2 m thick with a geometric mesh expansion factor of 1.15 for the levels above. For the simulations containing turbines, the Windmodeller built-in mesh adaption algorithm was selected for a finer mesh around the turbines. This includes approximately 15 cells across a 154 m diameter rotor, corresponding to approximately 10.3 m per cell (Appendix B). Mesh refinement restriction was applied

370 around the turbine actuator discs, to avoid an unnecessarily fine mesh away from the turbine locations, thus reducing numerical noise and computational cost.

The simulations used in the current work are summarised in Table 2.

375 **3 Results and discussion**

3.1 Trapped Lee Waves

The results from TLW simulations in this section are a snapshot from when the simulations reached a steady state with standing waves. For all simulations, the inlet windspeed is 12.5 ms^{-1} at a reference height of 106 m. However, the windspeeds just

380 upstream of the wind farm vary due to flow evolution throughout the domain with differing atmospheric stability conditions interacting with terrain and turbines. For comparison of windfarm inflow conditions, near upstream windspeed (U_{N7}, Fig. 9) refers to windspeeds at a point 300 m upstream of the bottom row of WMR before the blockage effect occurs (x = 0 for 41.4 km domain, Fig. 9). The wind farm blockage effect varies under the different stability conditions described in sections 3.1-3.3. The labels in Fig. 9 illustrate the different influences on U_N.
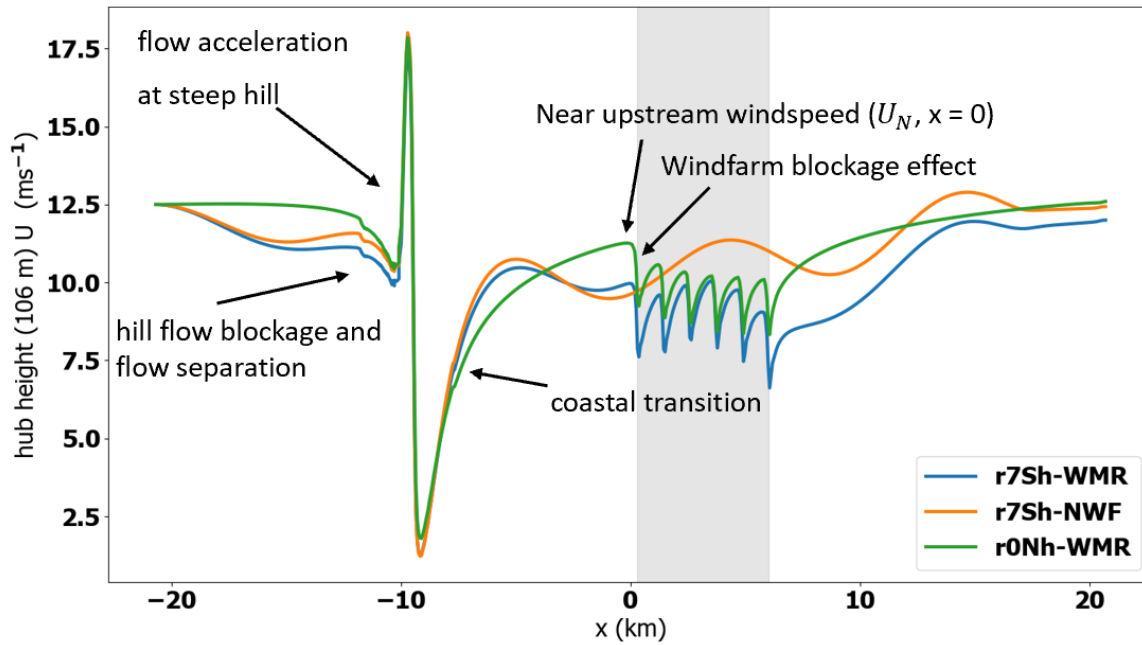
Figure 9. Wind farm and stability impacts on the flow. Values are at 106 m above the surface showing the TLW peak case at WMR (r7Sh-WMR, orange line), the TLW case without a wind farm (7Sh-NWF, blue line), neutral control with WMR (r0Nh-WMR, green line). Grey shaded region shows the x location of WMR wind farm.

Due to the variation in the values of U_N for the different simulations, direct comparisons between the simulation U_{us}, power, inflow angle and TI are complicated by different turbine thrust values. Absolute values are not compared in the current work, but the relative flow and power properties will still be influenced by differences in location on the turbine thrust and power curves at the given windspeeds. Despite this limitation, these results demonstrate topographical TLW impacts on flow patterns and consequent power outputs across WMR. Some of the influences on both U_N and turbine windspeed and power which are difficult to decouple are discussed in sections 3.1-3.3 including: recovery from the topographical blockage effect, presence of topographic TLWs, TLW phase, capping inversion and surface stability impacts, coastal transition flow adjustment impacts, presence, or absence of upstream TLWs, and windfarm flow blockage effect.
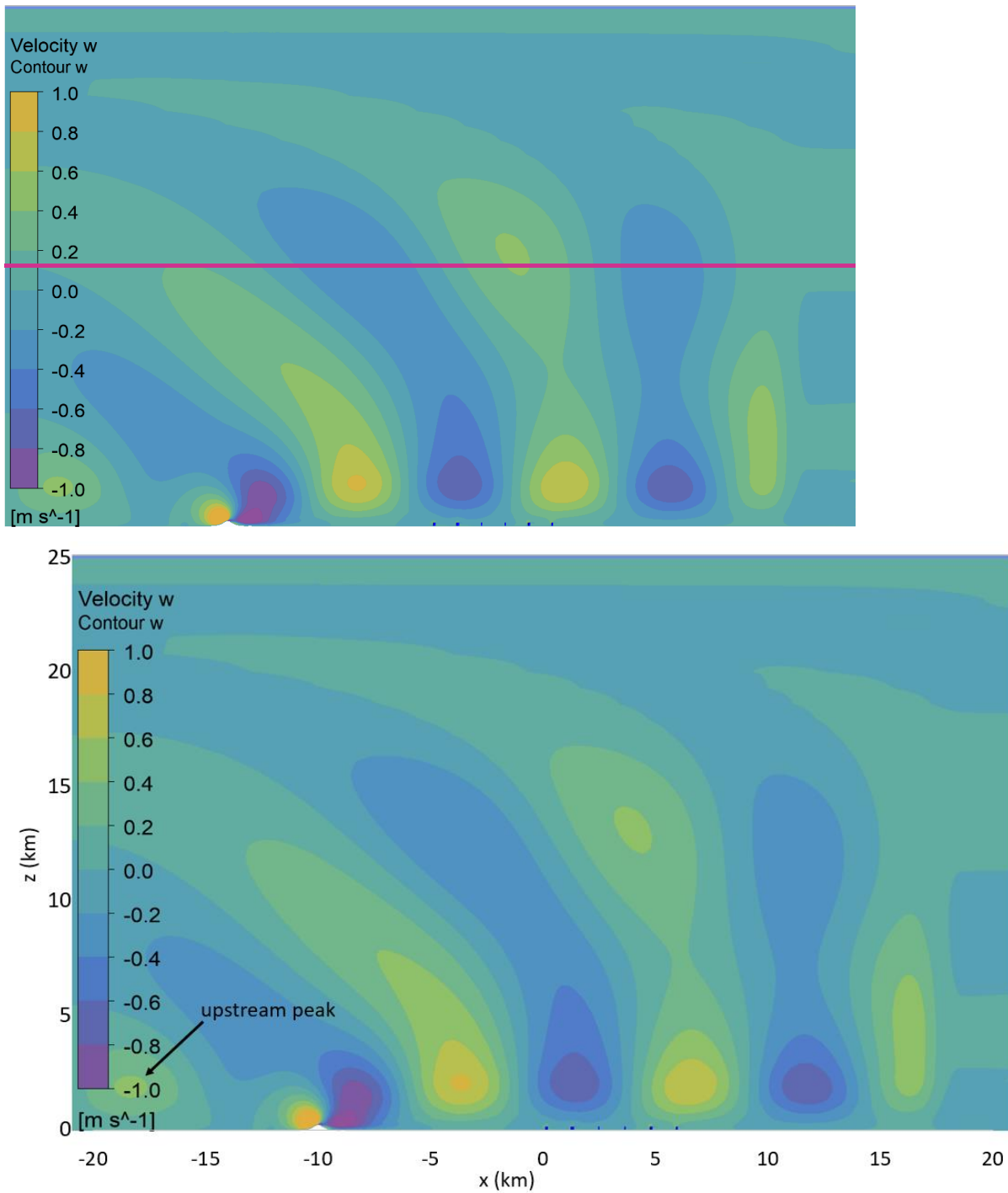
23
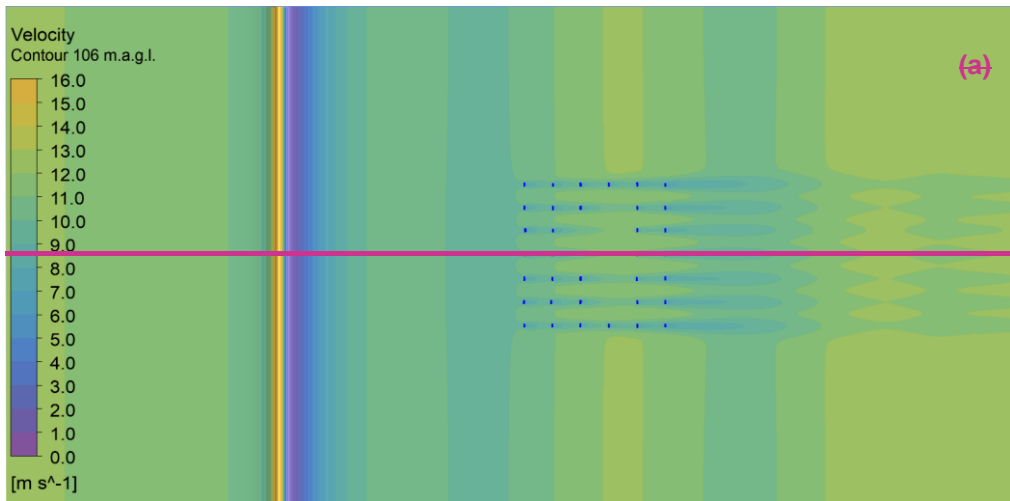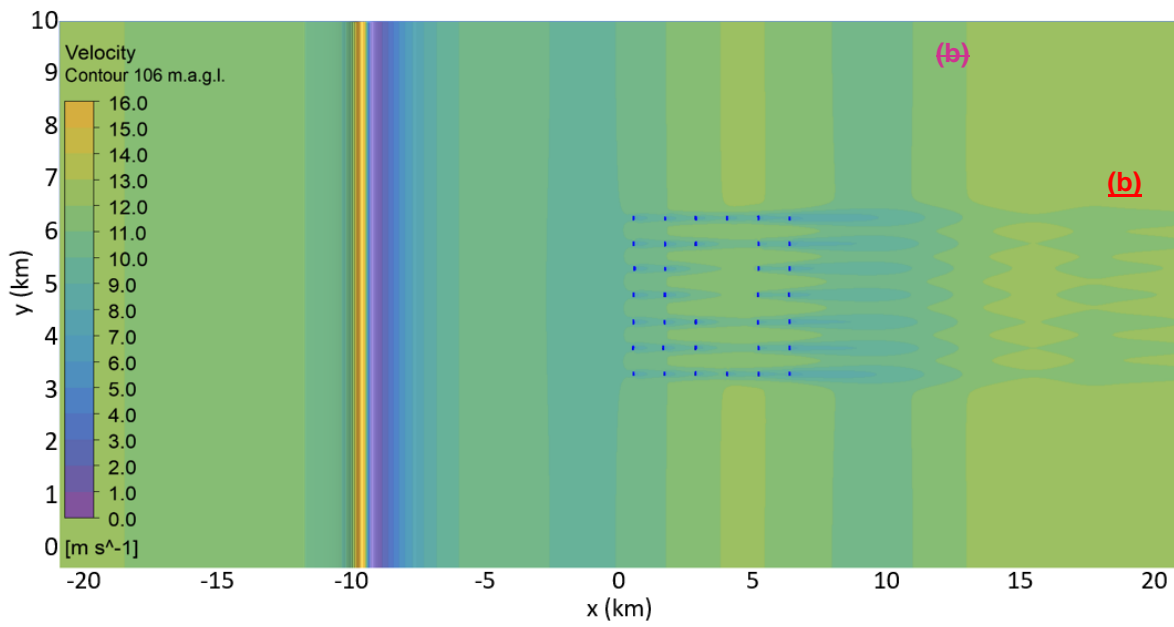
Figure 10. a) view from above: Horizontal velocity at 106m above the surface throughout the TLW (r7Sh-WMR) simulation domain. b) Side view: vertical velocity throughout the simulation domain the TLW (r7Sh-WMR) simulation aligned with the column 01 of WMR.

For the coastal hill simulations at WMR where $(\partial\theta/\partial z)_{inv} = 7.6$ K km^{-1} (r7Sh-WMR, r7Sh-NWF, Table 3.2), TLWs are observed downstream of the hill and persist throughout the domain to the outflow in both the horizontal velocity (Fig. 10a) and vertical velocity fields (Fig. 10b). Notably, there is a TLW peak upstream of the hill in Fig. 10b; TLW peaks also occurred in mathematical models of wind-farm induced TLWs where the Froude number (Fr, Eq. 23) was less than 1 (Smith, 2010; Lanzilao and Meyers, 2021).
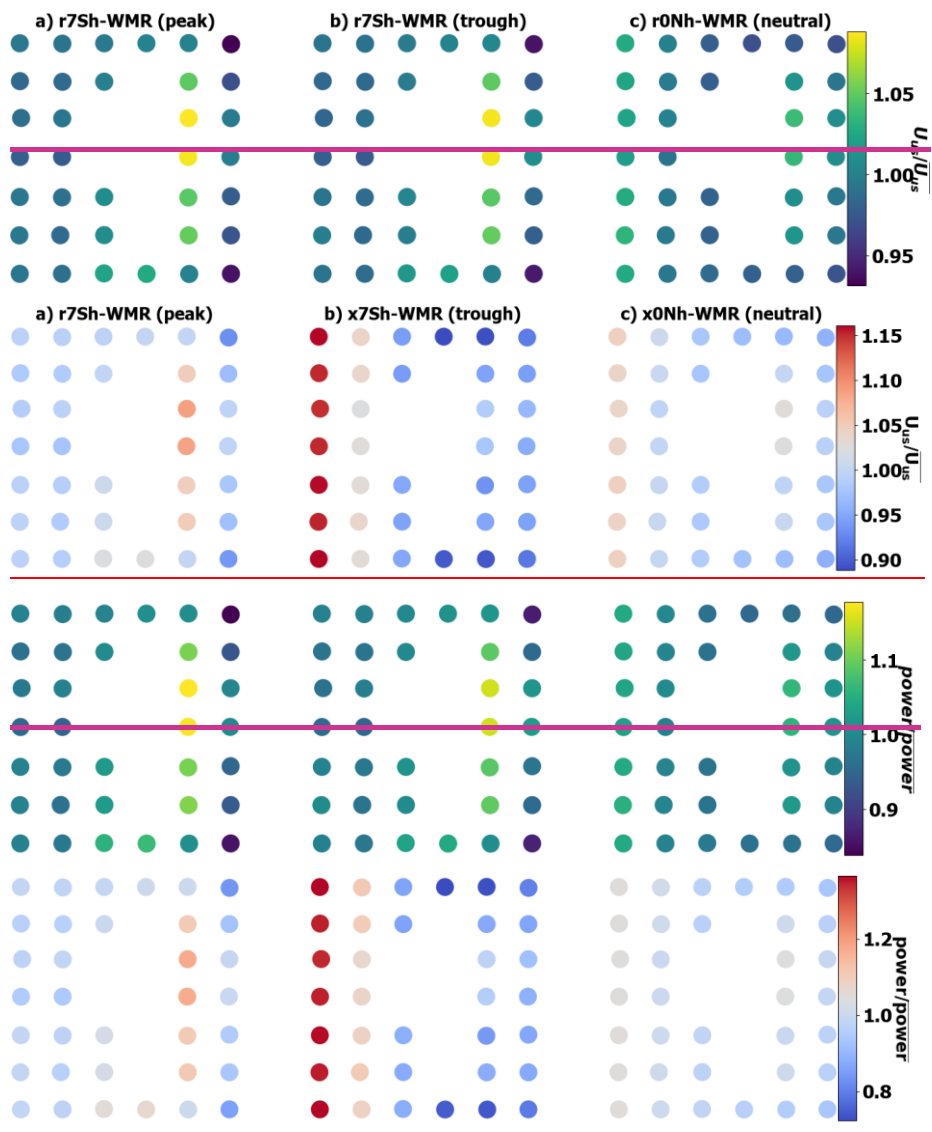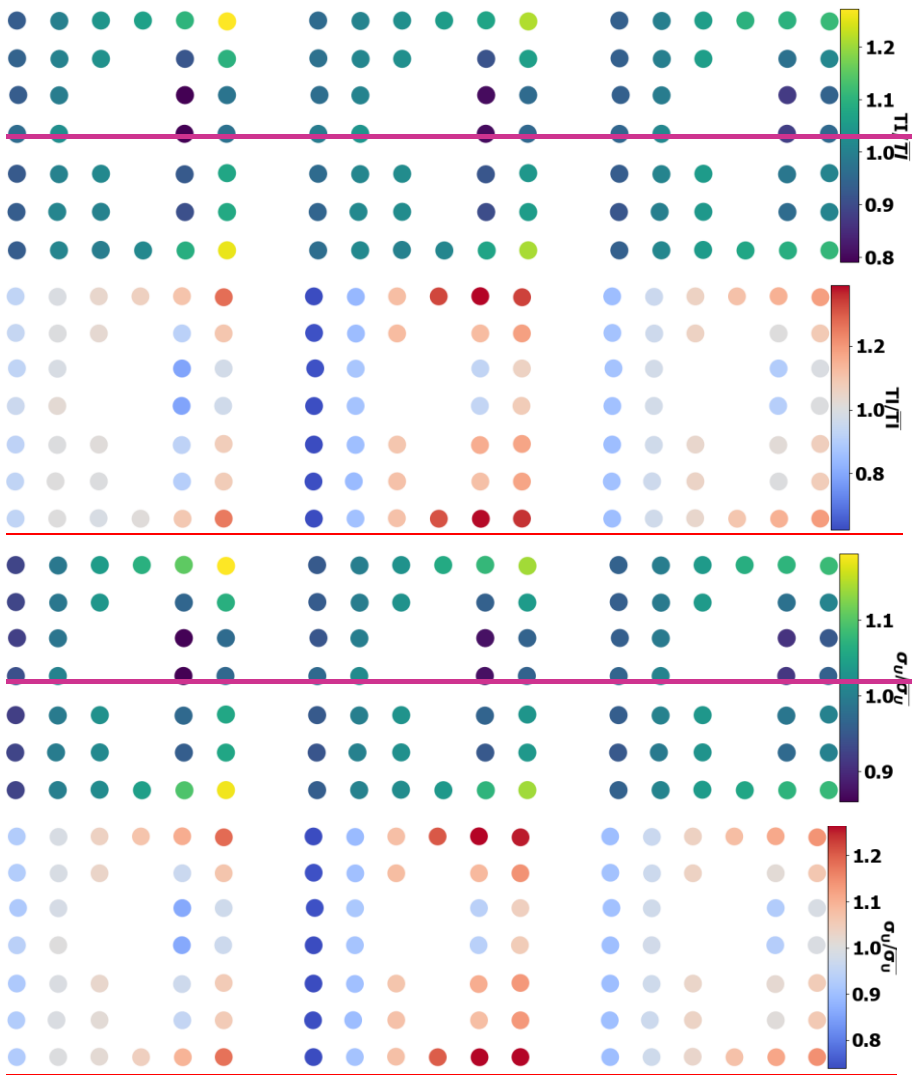
$$Fr = \left[\frac{U}{NH}\right] \qquad\qquad 23$$

Where U is mean windspeed (ms^{-1}), H is the obstacle height (m).

In the TLW cases (r7Sh-WMR, r7Nh-WMR) $Fr \sim 0.04$, ~~so the upstream wave behaviour is~~ consistent with ~~findings~~ upstream wave occurrence when $Fr < 1$ in previous studies (Smith, 2010; Lanzilao and Meyers, 2021). However, it is unclear at this stage whether the upstream peak is an artefact of imperfect wave damping and upstream domain length. The upstream peak is, however, considered far enough upstream of the windfarm to have negligible impact on the solution at WMR. The flow decelerates rapidly on approach to the steep hill ridge (slope ~33°, Fig. 3), with acceleration and flow separation at the peak and lee side (Fig. 10, Fig. 11). The flow separation is quite severe owing to the steepness of the hill. In the 41.4 km domain, the flow is still recovering from this deceleration upon approach to WMR. The TLW is superimposed on the recovering flow and has a gradually increasing windspeed (Fig. 10, Fig. 11a). The TLW characteristics are similar for the simulations with (r7Sh-WMR) and without (r7Sh-NWF) WMR wind farm, but the interaction with WMR results in overall lower windspeeds than when it is absent (Fig. 11a). TLW peak windspeeds are 11.4 ms^{-1} (r7Sh-NWF) and 10 ms^{-1} (r7Sh-WMR), with a mean difference of 0.94 ms^{-1} throughout the domain. The mean windspeed for the TLW case (r7Sh-WMR) is lower throughout the domain than for the neutral situation (r0Nh-WMR). In part this is due to the faster recovery from the hill wake in the neutral case (Fig. 11a). For reference, windspeeds for the neutral case (r0Nh-WMR) are included in Fig. 11. With a stable surface and capping inversion present (r7Sh-WMR) the flow recovery from the steep hill is slower so the TLW begins with a much lower windspeed than the neutral case. This discrepancy in U_N makes absolute comparison unclear. Further, it is not possible to fully decouple the impact of wind farm blockage effect under a strong $\partial\theta/\partial z_{inv}$ compared to neutral, where the blockage appears less (Fig. 11a). Two full TLW cycles are apparent in Fig. 10 and Fig. 11.

26
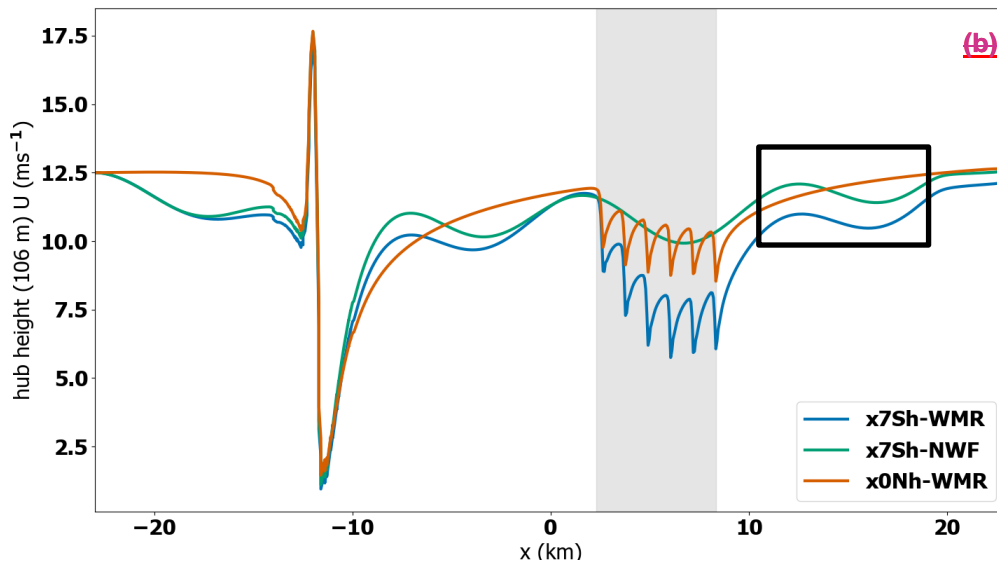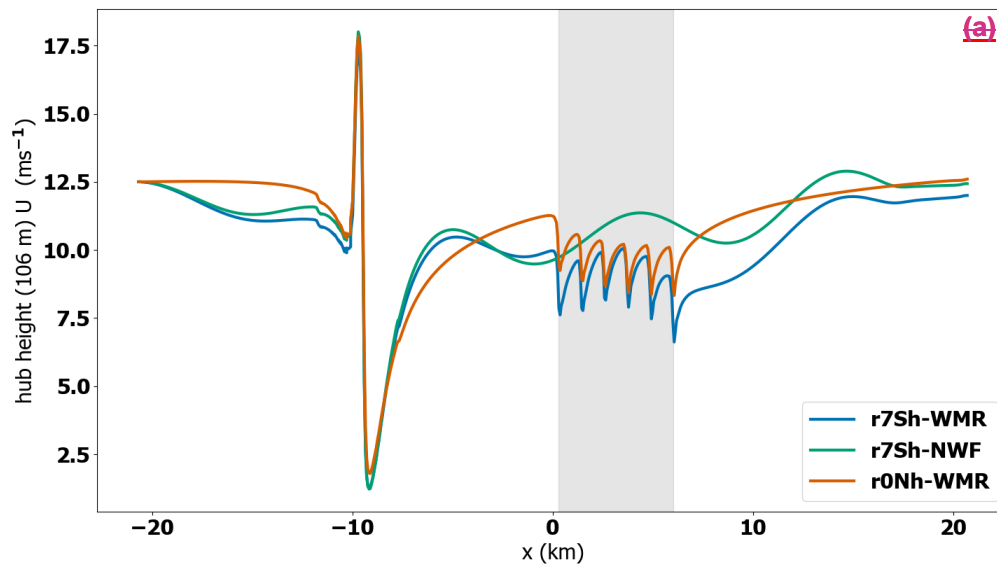
Figure 11. Wind speed at 106 m above the surface U (ms⁻¹)~~,~~). a) for TLW peak with WMR (r7Sh-WMR, blue line) TLW peak without wind farm (r7Sh-NWF, ~~orange~~green line) and neutral case with WMR (r0Nh-WMR, ~~green~~orange line) in the regular domain. b) 46 km domain for the TLW trough under the same conditions (x7Sh-WMR, x7Sh-NWR) and neutral case (x0Nh-WMR). Grey shaded region shows the x location of WMR wind farm. Black box highlights area of amplitude difference between TLW simulations.
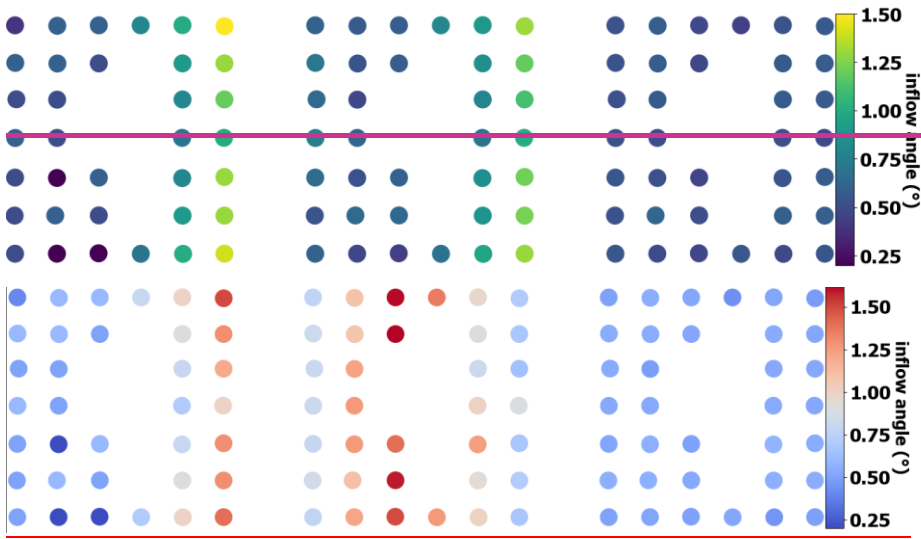
27

a) r7Sh-WMR (peak) b) r7Sh-WMR (trough) c) r0Nh-WMR (neutral)

a) r7Sh-WMR (peak) b) x7Sh-WMR (trough) c) x0Nh-WMR (neutral)

Figure 12. Values normalised to the mean for all turbines for U_{us} (ms⁻¹), power output, turbulence (σ_U) and TI and inflow angle (°) for the coastal hill domain. TLW peak (column a, r7Sh-WMR), TLW trough (column b, r7Nh-WMR) and neutral conditions (column c, r0nh-WMR)

—Here we introduce TLW impacts at WMR at the windfarm level by reviewing individual turbine and whole windfarm flow. Whilst both the neutral and TLW cases show recovery in windspeeds after the central gap in WMR (Fig. 12), the increase in windspeeds is much higher in the TLW case. The TLW has a maximum 10% increase in U_{us} (perpendicular velocity of the air cylinder upstream of the actuator disc) between turbines in row B and E either side of the gap in the TLW situation (r7Sh-WMR, ~~Fig. 12).~~Fig. 12). For the neutral situation (r0Nh-WMR) there is only 4% increase for the same turbine locations (~~Table 3).~~Table 3). The greater recovery is explained by the increases in windspeeds due to the TLW countering wake losses. However, the central gap in WMR makes the TLW effect less clear. Furthermore, the variability in U_{us} throughout WMR is considerably higher for the TLW case (r7Sh-WMR) than the neutral case, with the range of windspeeds experienced by the turbines over double that of the neutral simulation (Fig. 12, Table 3). The TLW range of U_{us} and power output across the farm are 2.1 and 2.4 times the neutral case respectively (Table 3). The power difference is greater due to the non-linear nature of the power and thrust curves. There are also coincident greater increases in turbulence and local TI (Eq. 20) at the turbines when the TLW is present (Fig. 12), as the trend is the same for both parameters this is attributed to more variable vertical velocity and shear in the TLW situation which are influenced by the coupled impacts of the TLW and the capping inversion (Appendix C).

Column 01 of WMR, where there is no gap between turbines, is less affected by adjacent columns under the 270° wind. This column shows the clearest TLW signature (Fig. 12a~~).~~). Throughout this column, the range of U_{us} values is 0.9 ms⁻¹ for the TLW case compared to 0.6 ms⁻¹ in the neutral case. For the same locations, mean U_{us} is 1.2 ms⁻¹ less for the TLW case than neutral. The range in power output down column 01 for the TLW is over double the neutral case (1000 kW, 472 kW,

455   respectively). This is due in part to differences in windspeed position on the thrust and power curves between the simulations

      exaggerating the windspeed differences.

Table 3: Simulation descriptive statistics for all WMR turbines for U_{us}, power, TI, inflow angle and shear exponent factor (α).

460

		r0Nh-WMR	r7Sh-WMR	r7Nh-WMR	x7Sh-WMR	r3Nh-WMR	x0Nh-WMR
U_{us}(ms^{-1})	mean	11.4	10.7	10.9	10.2	10.2	11.7
	max	11.8	11.6	11.9	11.9	10.7	12.3
	min	11.1	9.9	10.3	9.1	9.7	11.2
	range	0.8	1.7	1.6	2.8	0.9	1.1
	std	0.2	0.4	0.3	0.9	0.3	0.3
Power (kW)	mean	5400	4700	5000	4200	4200	5600
	max	5700	5500	5700	5700	4700	5900
	min	5100	3900	4300	3000	3700	5200
	range	600	1600	1400	2700	1000	700
	std	200	300	300	900	300	200
	total	188200	164200	174100	146600	147100	196000
Turbine TI	mean	0.18	0.18	0.18	0.24	0.19	0.16
	max	0.20	0.23	0.22	0.18	0.23	0.19
	min	0.16	0.14	0.15	0.25	0.16	0.13
	range	0.04	0.09	0.08	0.11	0.07	0.05
	std	0.01	0.02	0.02	0.14	0.02	0.02
σ_u	mean	2.0	1.9	2.0	1.8	2.0	1.8
	max	2.2	2.3	2.3	2.3	2.3	2.1
	min	1.8	1.6	1.7	1.3	1.7	1.6
	range	0.4	0.6	0.5	1.0	0.5	0.5
	std	0.1	0.1	0.1	0.3	0.2	0.1
Inflow angle (°)	mean	0.53	0.74	0.77	1.03	0.83	0.52
	max	0.63	1.50	1.31	1.62	0.93	0.58
	min	0.45	0.20	0.44	0.64	0.73	0.43
	range	0.17	1.30	0.87	0.98	0.20	0.14
	std	0.04	0.34	0.25	0.29	0.06	0.03
α	mean	0.13	0.18	0.18	0.21	0.17	x0.12
	max	0.18	0.25	0.26	0.37	0.24	0.16
	min	0.10	0.12	0.11	0.09	0.12	0.08
	range	0.08	0.14	0.15	0.28	0.12	0.09
	std	0.02	0.04	0.04	0.07	0.03	0.02

3.2 Location of WMR in TLW wave cycle

Whilst the wave behaviour is similar in the 41.4 km domain (r7Sh-WMR) and the extended 46 km (x7Sh-WMR) domain, the flow characteristics at WMR are notably different depending on where the TLW hits the wind farm (Fig. 11). Turbine windspeeds and wakes in column 01 of WMR increase and decrease in phase with the TLW. In both cases, the TLW shape is
465   clearly superimposed on the turbine windspeeds, despite the wind farm blockage effect and the fluctuation within the wind farm due to wake losses (Fig. 11). With stable surface conditions, wake recovery is slower, yet the TLW reduces the impact of the wake losses when windspeeds increase towards the peak of the wave, counteracting some of the surface stability influence (r7Sh-WMR, Fig. 11a). Wake losses are, however, amplified towards the TLW trough (x7Sh-WMR, Fig. 11b).

When the TLW is reaching its trough (x7Sh-WMR, Fig. 11b), TLW reduction in windspeeds compounds the reduction in
470   wind speed due to the wake losses so the windspeeds are dramatically reduced. These windspeed reductions are much more pronounced than the reductions after the TLW peak in r7Sh-WMR. This is explained by differences in nU_{us} between simulations. The turbines in the trough case experience the trough windspeeds at a steeper location on the thrust curve leading to deeper wake losses. At the wind farm level (Fig. 12), mean U_{us} is reduced relative to the neutral situation in both the peak and trough situations, as even in the peak case the first turbine row (row A) is in the recovery from an upstream TLW trough.
475   Here with the same far upstream conditions, but the TLW hitting the wind farm at a different part of the wave cycle, the range in windspeeds is 1.7 times the range for trough compared to peak case (Table 3.3); this difference is of the same order as the difference between the peak TLW and the neutral case. The difference in U_N is 1 ms^{-1}, so the windspeed range difference is explained mainly by the wave positioning, exaggerated by operating at a different point on the thrust curve, rather than the U_N alone.

480   In the extended domain, the neutral simulation has a slighter higher U_N compared to the TLW case (11.9 ms^{-1} and 11.7 ms^{-1}, respectively, Fig. 11b). This is due to the longer distance between the hill and WMR allowing for further windspeed recovery from the steep hill. Consequently, there is also a much smaller difference in U_{us} (mean 0.4 ms^{-1}) in turbine column 01, between the TLW (x7Sh-WMR) and neutral case (x0Nh-WMR), than in the regular domain. Therefore, it is possible to directly compare the windspeeds between the two cases. The large range in U_{us} throughout WMR for the TLW situation (2.8 ms^{-1}, x7Sh-WMR,
485   Table 3.3) is mainly accounted for by the atmospheric conditions rather than differences in initial U_{us}, with a mean difference of 1.4 ms^{-1} at WMR between the two cases. The large range in U_{us} could be attributed to increased wake losses due to the stable surface conditions and the strong capping inversion aloft rather than the TLW itself.

At the wind farm level (Fig. 12) the TLW signature is most clearly seen down column 01 of WMR in both cases, which is less affected by the gap within the centre of the wind farm. The wave pattern is subtly apparent throughout all the turbine rows
490   with U_{us} and subsequent power output rising and falling in phase with the TLW cycle (Fig. 12). TI varies more in both the peak (TI range 0.09) and the trough cases (TI range 0.11) with both ranges over double the neutral case (TI range 0.04, Table 3). The changes in TI have a similar distribution to the changes in turbulence, suggesting that the range of turbulence is a result vertical velocity changes in the TLW rather than windspeed differences. As the vertical velocity is more variable during TLW

flows, so are the inflow angles compared to neutral conditions (see Table 3 and Fig. 12). Notably, the TI, shear and turbulence
495   are higher in the peak case for turbines F01 and F07, this is discussed in Appendix C.

Regardless of where in the wave cycle the TLW interacts with WMR, it recovers and the wave train persists after interaction
with WMR with a slight reduction in windspeed compared to the no wind farm scenario (r7Sh-NWF, x7Sh-NWF, Fig. 11).
The TLW appears to flatten at the domain outlet, but this is due the outlet wave damping. This suggests the same topographical
TLW may cause deviations from predicted power output for multiple wind farms downwind of the same hill or coastline. This
500   is similarly discussed for onshore wind farms in (Draxl et al., 2021). However, due to the domain length here, it is not possible
to see how far the TLW wave-trains persist and how much windspeeds recover downstream.

These results demonstrate the TLW impact on the flow, U_{us}, power, TI, and inflow angles throughout WMR, but to
understand the impact it is essential to determine which part of the wave cycle the wind farm is in when experiencing
quasi-stationary gravity waves. The impacts of the TLW will fluctuate in severity across the wind farm with TLW phase. As
505   location in the TLW phase has such a pronounced impact, this suggests the wind farm dimensions and turbine spacing will
also be important as they will affect how much of the wind farm is within the TLW. Similarly, the wavelength and amplitude
will determine what proportion of a given wind farm is in the different TLW phases and how severe the windspeed changes
are.

WMR interaction with the TLW appears to have negligible impact on wavelength; the distance between the TLW peak in
510   the WMR centre (grey shaded region, Fig. 11a) and the first peak after the WMR the wavelength is ~10.7 km for both the
WMR and NWF situation at 600 m.a.s.l. away from the turbine rotors. This is also the case for the TLW trough situations.
This is comparable to the wavelength predicted from the upper layer Scorer parameter (l^2, Eq. 24-25, ~12 km).

$$\lambda = \frac{2\pi}{l(z)}$$

24

$$l^2(z) = \frac{N^2}{U^2} - \left(\frac{\partial^2 U}{\partial z^2}\right) / U$$

25

Where λ is wavelength, $N = N(z), U = U(z)$ is the vertical profile of the horizontal wind.

There are apparent reductions in TLW amplitude where WMR is present compared to the NWF simulations. However,
515   these differences are superimposed on flow recovery and wind farm blockage effects. The difference is most clearly observed
in the black box in Fig. 11b where the peak-trough amplitude windspeed difference is 0.7 and 0.5 ms^{-1} for x7Sh-NWF and
x7Sh-WMR, respectively. Amplitude reduction is also observed upstream of WMR in Fig. 11a,b. As the TLW persists with
reduced amplitude after interaction with WMR, this suggests that a TLW event affecting multiple farms may have less impact
on windspeed and power fluctuations if there is another windfarm upstream.

520

3.3 Surface layer stability impacts

Whilst the section above discusses the impact of a temperature inversion with stable surface layer (r7Sh-WMR), this section investigates whether the stable surface layer has a strong effect on the variation of windspeeds across the wind farm. For r7Sh-WMR the stable surface layer has less impact than might be expected as the profile becomes neutralised as it evolves through the domain (Fig. 13b). Using Monin-Obukhov Similarity Theory (Eq. 26) and taking $\frac{z}{L}$ across blade tip heights (29-183 m) between the inlet and hill (line 1, Fig. 13), gives $\frac{z}{L}$ = 1.09 and L = 96.9 m suggesting the flow is very stable.

$$\frac{z}{L} = Ri_G \qquad\qquad 26$$

where z is height, L is the Obukhov length and Ri_G is the gradient Richardson number.

Yet the stability profile has a relatively subtle temperature offset once the inlet profile has adjusted within the domain and interacted with the topography to a relatively small temperature offset (< 1 K) and shallower surface layer (lines 2-11, Fig. 13b). Changes in velocity profile after the topography may be attributed to TLW trough flow effects on shear and associated turbulence as described in Vosper et al., (2018). To obtain a temperature profile with strong stability at WMR the Windmodeller inlet surface temperature offset would need to be increased to counteract the neutralisation in the domain.
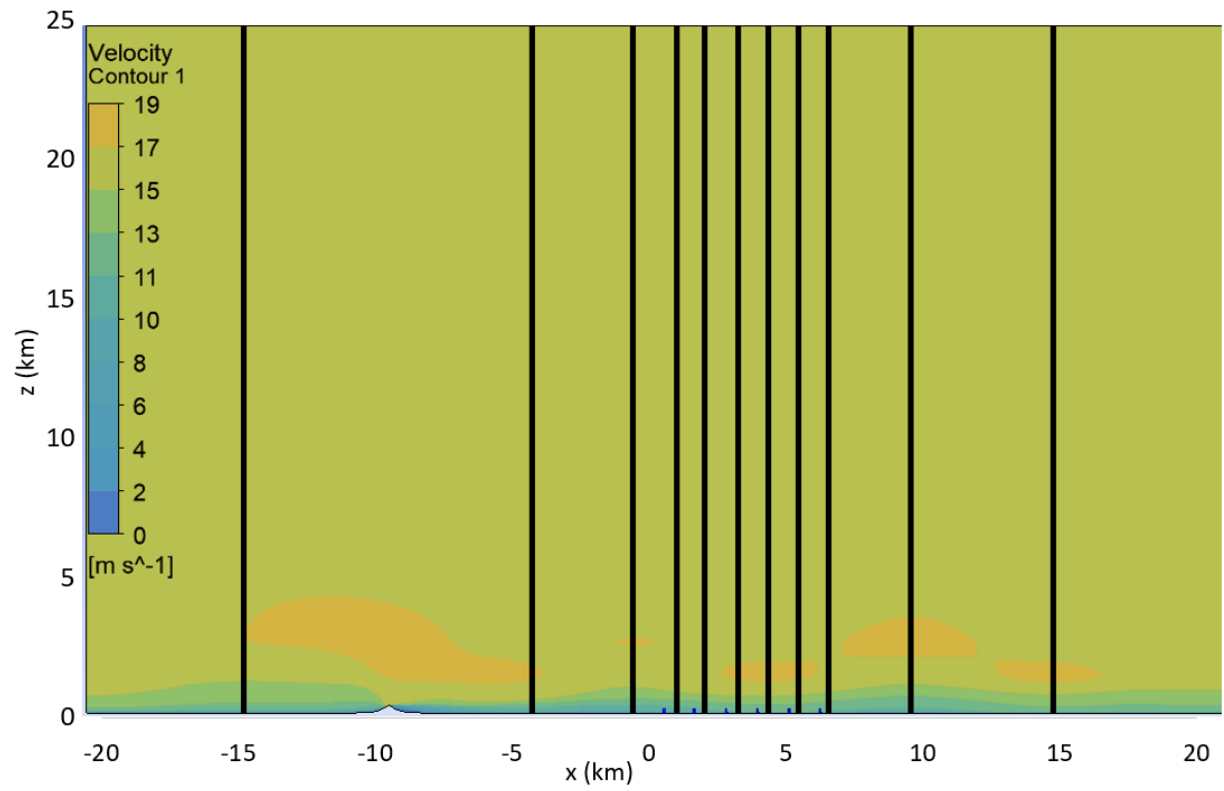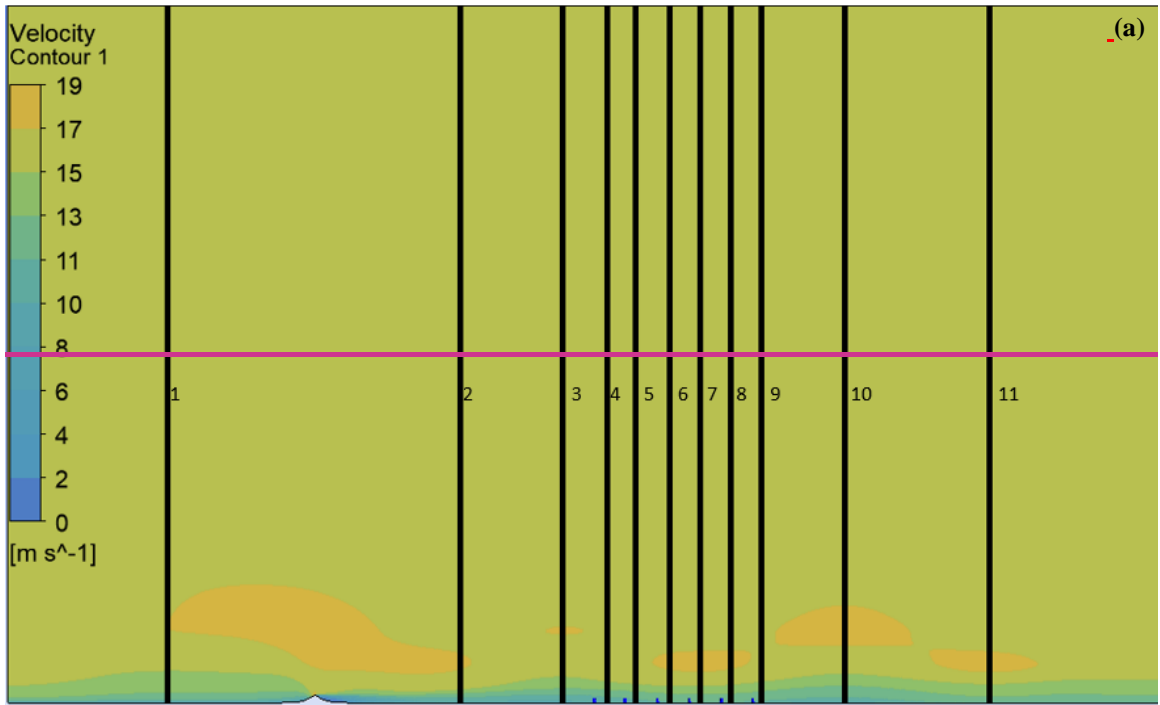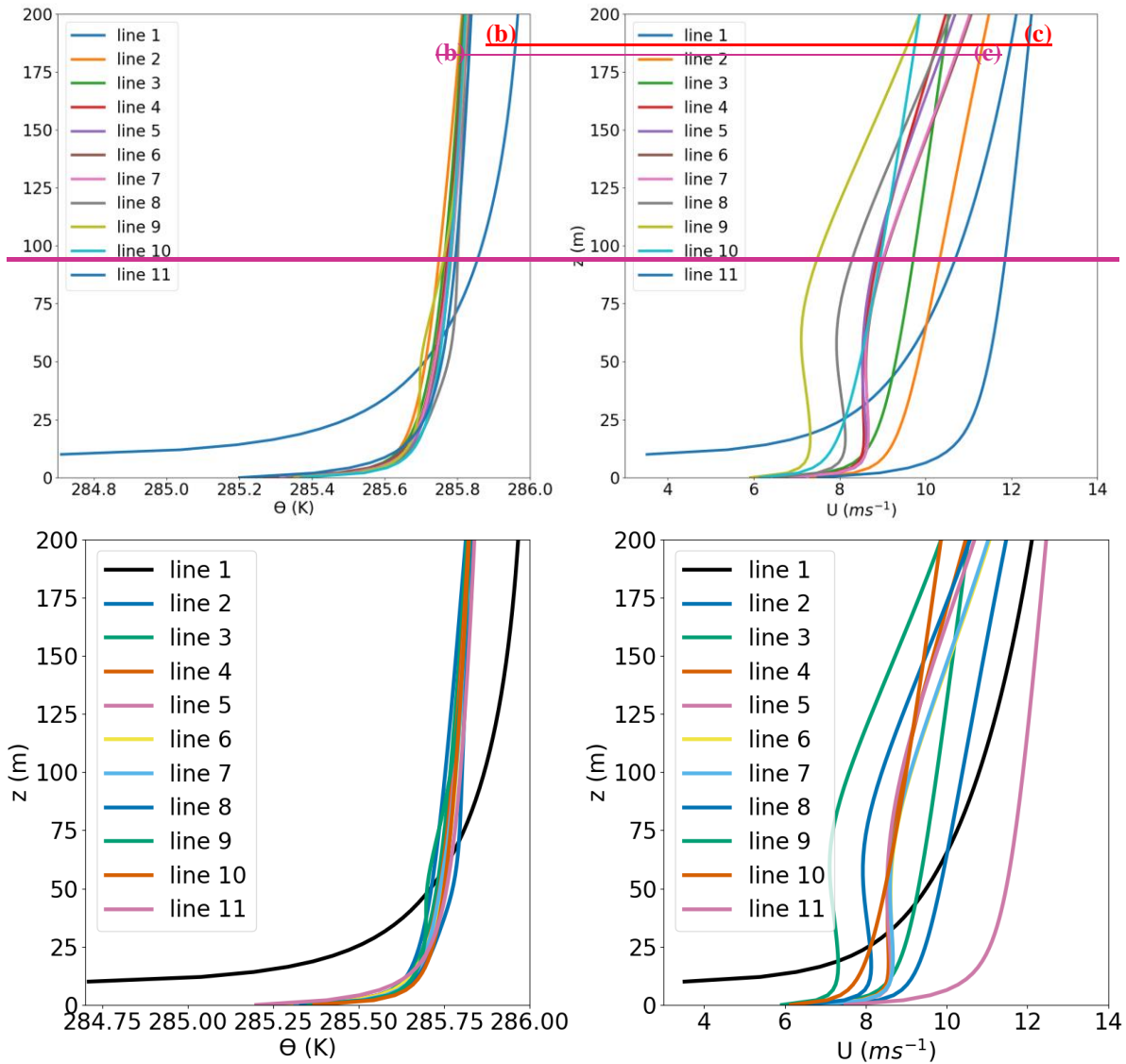
35

Figure 13. a) vertical slice through the domain in line with column 01 of WMR turbines showing vertical velocity for the ~~AGW~~TLW case (r7Sh-WMR). Yellow lines represent are lines 1 –11 as labelled in all 3 plots. Below: WM potential temperature (b) and velocity (c) profile for lines 1-11.

As shown in Fig. 14, the flow throughout the domain is similar for both the inversion case with the neutral surface layer (r7Nh-WMR) and stable surface layer (r7Sh-WMR~~).~~). With the stable surface layer (r7Sh-WMR), mean U_{us} and power are reduced with increased wake losses slightly increasing the windspeed reduction effect of the ~~AGW~~TLW. This leads to negligible increases in variation in U_{us} with a range of U_{us} which is 0.07 ms^{-1} greater for r7Sh-WMR than for the neutral surface layer

37

(r7Nh-WMR) with resulting power output variation range of 1592 kW (for r7Sh-WMR) and 1435 kW (for r7Nh-WMR) (Table 3, Fig. 14, Fig. 15).

545   The influence of the ~~AGW~~TLW dominates with a slight reduction in the range of values for all variables for r7Nh-WMR compared to the stable surface layer case (r7Sh-WMR, Table 3). Fig. 15 compares the whole wind farm for the stable surface and neutral surface cases (power, TI, U_{us}) with neutral conditions for the regular domain. As the surface stability temperature offset reduces substantially after interaction with the topography and sea surface (lines 2-11, Fig. 13), the stable layer is relatively shallow with the surface lapse rate increasing to near neutral conditions around rotor height. Thus, the differences

550   between r7Sh-WMR and r7Nh-WMR are relatively subtle. In these situations, the impact of the capping inversion appears much more important than the surface stability. Yet, much larger differences between the stable and neutral surface layer simulations would be expected with a stronger and deeper stable layer at the surface which would increase wake losses further.
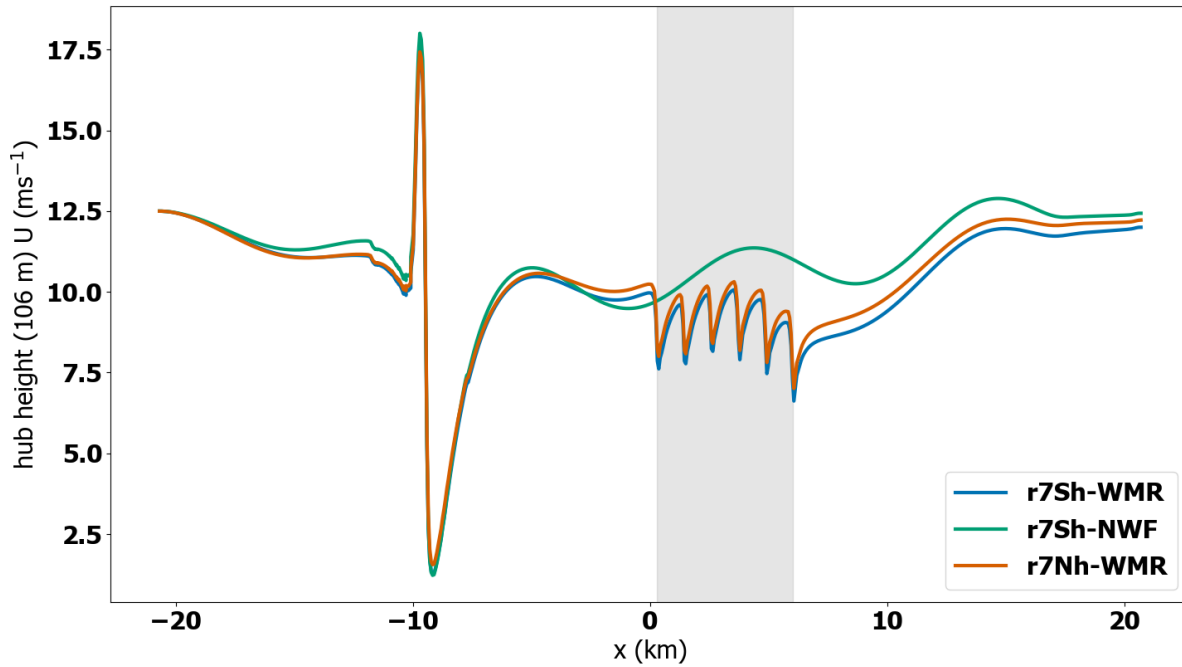
Figure 14. 106 m above the surface isolines of U aligned with column 01 of WMR for capping inversions with (r7Sh-WMR, orange
555   **line) and without (r7Nh-WMR, blue line) stable surface conditions and stable surface conditions without WMR (r7Sh-NWF, green line).**
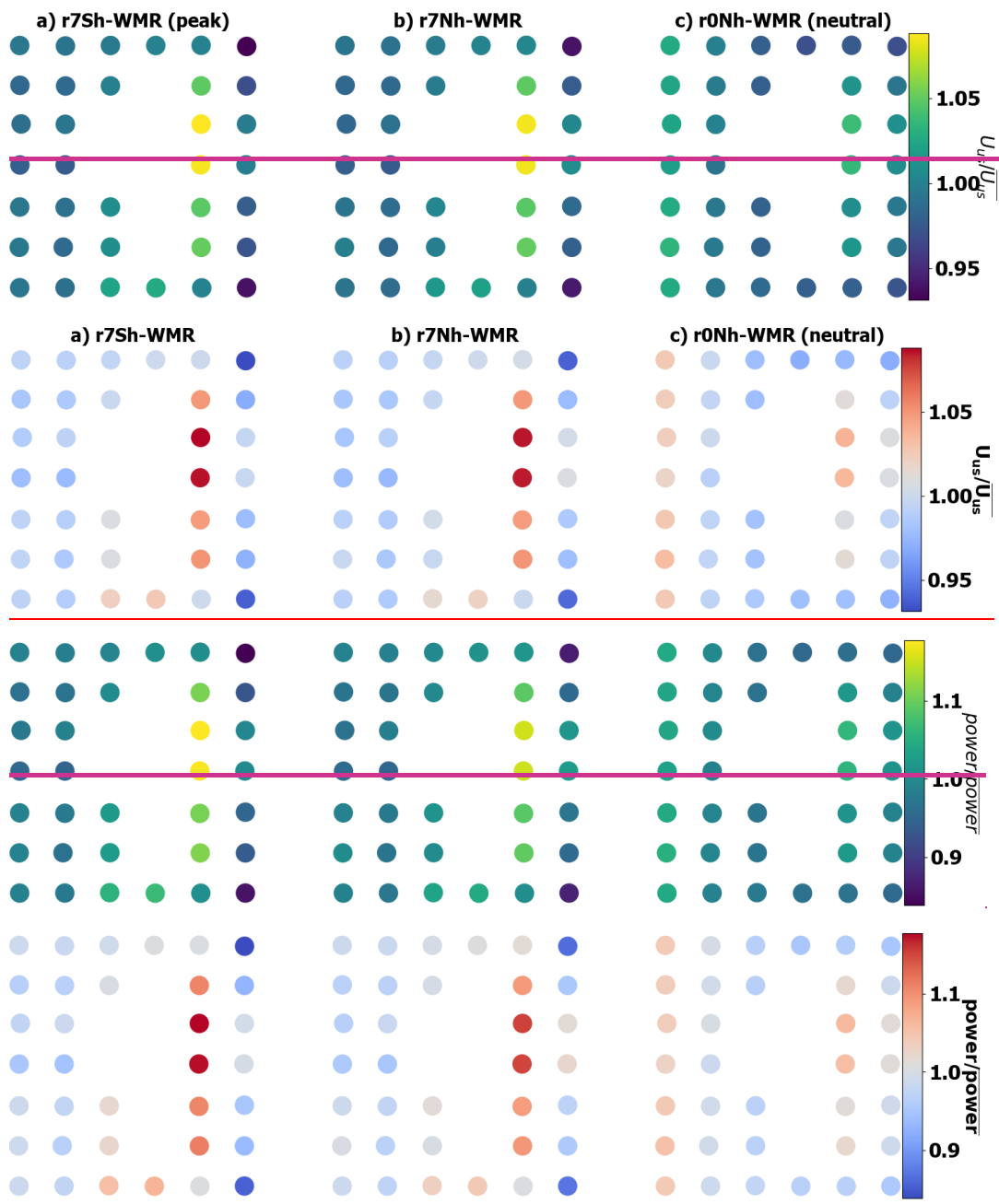
Figure 15. View from above WMR, normalised to the mean value for WMR for U_{us} and power output (kW) for the ~~AGW~~**TLW** peak (column 01, r7Sh-WMR), ~~AGW~~**TLW** peak CNBL (column b, r7Nh-WMR), and neutral (column c) r0Nh-WMR) cases.

3.4 TLW compared to CNBL conditions at WMR

560

The CNBL case (r3Nh-WMR) is a more realistic atmospheric situation than purely neutral conditions (r0Nh-WMR). In Fig. 16a U_N for r3Nh-WMR is substantially higher than for the TLW peak situation (r7Sh-WMR, 10.9 ms^{-1}, 9.6ms^{-1}, respectively at x=0). However, the gradual decline in windspeeds due to wake losses reduces U_{us} throughout WMR to less than those for the TLW situation (r7Sh-WMR, b), where the losses are countered by the peak of the TLW. The reduced windspeed in the

565 CNBL case (r3Nh-WMR) results in a lower position on the power curve, resulting in a reduced power output across WMR compared to the TLW peak and neutral cases (Fig. 16). Whilst U_{us} and power are more variable for the TLW situation (r7Sh-WMR, range 1.8 and 2.7 times greater, respectively, Table 3) than for the CNBL, the total power output is only 1.1 times lower for the CNBL case (r3Nh-WMR) due to its higher U_N. Whilst these differences are small, if U_N were equal for both cases, i.e., different far upstream windspeed, the TLW would cause more dramatic increases in power output compared to the control as

570 the initial offset between the two cases would be removed. U_{us} and power increases would be expected as the peak increases are not counter-balanced by the TLW troughs, as WMR is small and is not experiencing the lowest speeds in the TLW trough in this situation (Fig. 16). Not accounting for differences in atmospheric stability and TLW impacts could result in over or underestimation of power output when based on a mast measurement alone.

The CNBL case is approximated to real conditions at WMR so is more representative than purely neutral conditions,

575 however, what constitutes a true control for TLW situations is unclear. Here the CNBL has a shallow and weak inversion. Modifications to height, depth and strength of inversion layers will produce different windspeeds and turbulence throughout the domain and interact differently with individual turbines and whole wind farms. As discussed in section 5, investigating TLWs using a variety of stability profiles, and producing control simulations with varying profiles and similar near upstream windspeeds would be beneficial for full quantification of TLW impact.
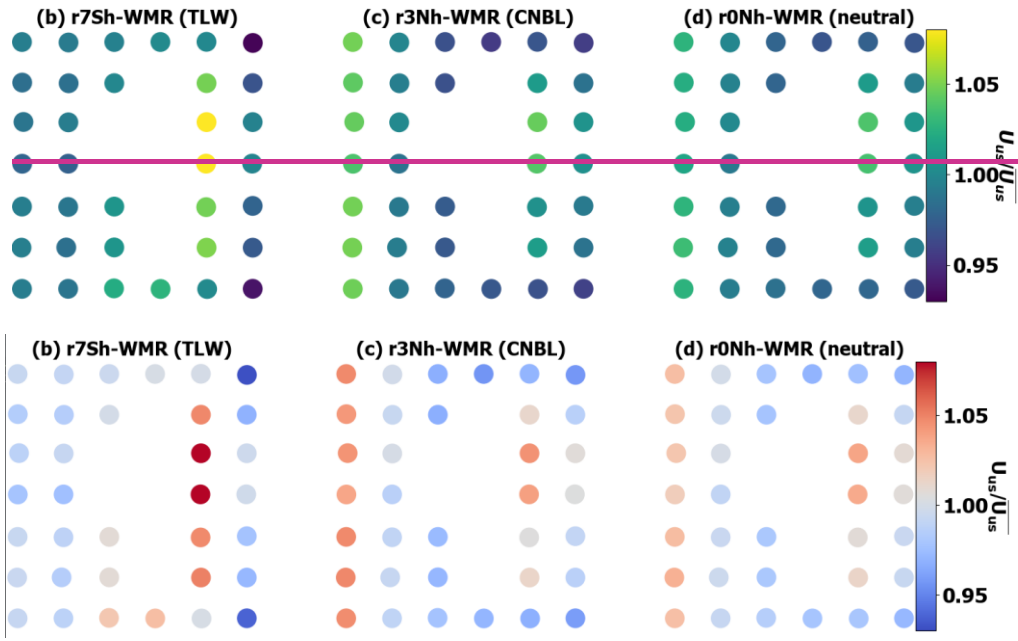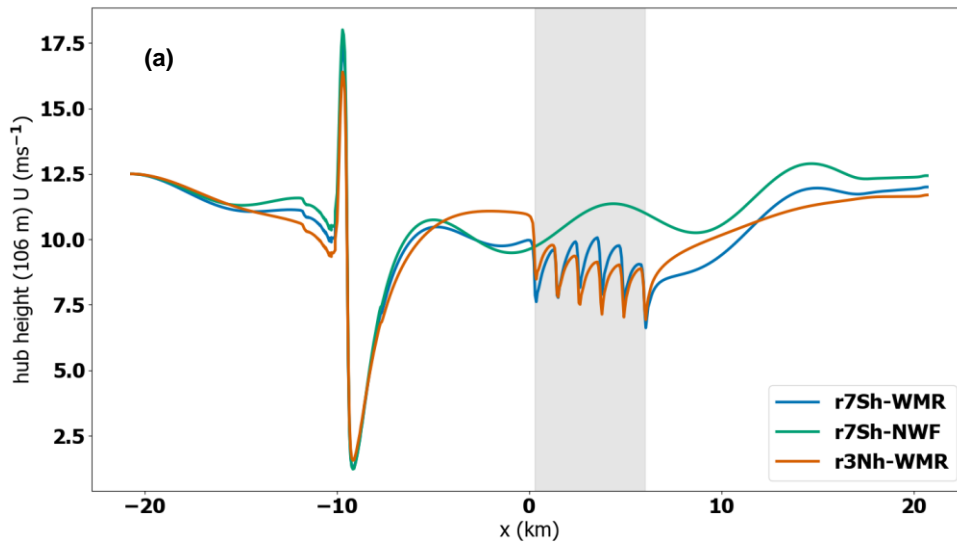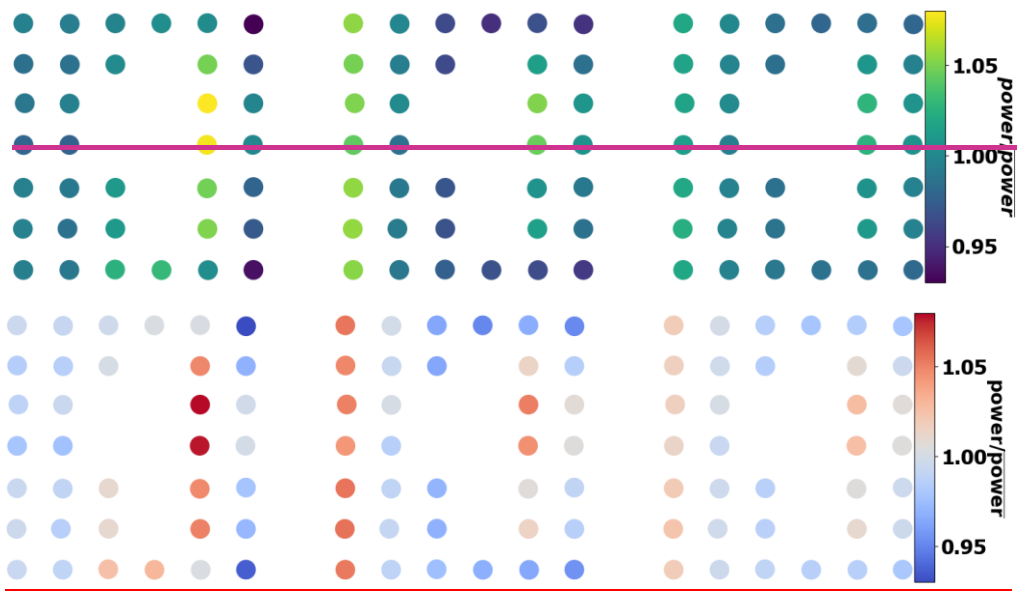
Figure 16 a) hub height windspeed aligned with column 01 of WMR for TLW (r7Sh-WMR, blue line), TLW without WMR (r7sh-NWF, orange line) and weak CNBL case (r3Nh-WMR, green line). Below: Normalised U_{us} and Power for WMR for TLW (column b, r7Sh-WMR), CNBL (column c, r3Nh-WMR) and neutral cases (column d, r0Nh-WMR).

3.5 Impact of ~~AGW~~TLW on potential turbine loading for topographical ~~AGW~~TLW simulations

585

For all the topographical TLW simulations at WMR (r7Sh-WMR, r7Nh-WMR, x7Sh-WMR), the range of inflow angles is larger than for the neutral equivalents (r0Nh-WMR, x0Nh-WMR, Fig. 12~~).~~). Mean inflow angle is largest for the TLW trough simulation (x7Sh-WMR) where it is almost double that of the neutral equivalent (x0Nh-WMR) (mean 1.03°, 0.52°, range 0.98°, 0.14° respectively, Table 3). Whilst the TLW inflow values are higher, they are well within the tolerance range of

590 modern wind turbines ($\leq \pm 8°$) so turbine fatigue loading does not seem to be a concern for these conditions. The TLW trough simulation (x7Sh-WMR) also shows the largest difference in turbine TI compared to the neutral case (r0Nh-WMR, mean 0.24, 0.16, range 0.11, 0.05 respectively). As the trends in turbulence and TI match, the changes in TI are likely a result of shear associated with up and downslope TLW flow.

Whilst this research focuses on the impact of TLWs on U_{us} and power output, larger inflow angles, greater TI and associated

595 shear suggests that some turbines across the wind farm are likely to experience greater fatigue loading during TLW events and that this is not uniform across the wind farm. However, these increases in inflow angle and TI do not appear large enough to substantially impact turbine fatigue and lifetimes.

4 Conclusions

600 Topographical TLW interaction with wind farms is common and has, until recently, been overlooked. In this parametric study, turbine and whole wind farm windspeeds and power outputs behaved differently in the presence of topographically forced TLWs. In the simulations, the reference windspeed at the inlet was analogous to a mast measurement taken 20 km upstream of a proposed wind farm site. In the presence of an upper layer inversion, strong TLWs meant the topographical influence was more apparent. These results demonstrate that with the same apparent synoptic forcing conditions, local

605 conditions favouring TLW formation may lead to large deviations between the predicted and actual wind speed. Thus, power output from individual turbines and whole farms will vary significantly from predicted if these conditions are not accounted for. Greater variability in local turbulence and shear was also apparent during TLW situations attributed to TLW and capping inversion impacts on wake and shear. However, the TLW impact on inflow angles within WMR, were well within the tolerance of modern wind turbines. TLW events affecting multiple windfarms may have less impact on power output for windfarms

610 downstream of an existing windfarm due to appreciable reductions in TLW amplitude with windfarm interaction.

The different atmospheric stability conditions led to the same upstream flow conditions interacting very differently with the topography upstream of the wind farms. Consequently, windfarm inflow speeds were highly variable between TLW and non-TLW events leading to differences in windspeed throughout the windfarm. These differences were further complicated by the varying windspeed recovery from the coastal transition and differences in wind farm blockage effects in different

615 stability regimes. Additionally, wake recovery appeared dependent on both the TLWs and strength of the capping inversions.

With these interacting conditions it was not possible to fully decouple which impacts on wind turbine and whole wind farm windspeeds and power were a result of TLWs and which were a result of different stability impacts on the flow.

When compared to purely neutral conditions throughout the domain, all the TLW simulations had reduced power output. These reduced speeds compared to neutral for TLW simulations were primarily due to reduced flow recovery after the hill due to stability differences. As it was not possible to define consistent wind farm inflow conditions between TLW and control simulations, it remains unclear how much of this influence was due to TLWs compared to impact of differing U_N. The effect will be situation dependent as differences in U_N lead to different operating points on the thrust curve and non-linear changes in wake losses. Yet, when compared to a non-TLW CNBL event at WMR, with higher U_N than the TLW, subtle increases in turbine U_{us} and turbine – whole wind farm power output were observed during the TLW. This suggests that TLWs may sometimes have beneficial impacts compared to real CNBL conditions. How the TLW impact is interpreted is largely based on what is taken as the 'control' situation. In all simulated cases, TLW events increased the variability in windspeeds and power outputs through the windfarm. Despite the variation in U_N which complicates the interpretation of the results, it is concluded that TLWs can have a substantial impact on the variation in wind speeds and TI experienced across an offshore wind farm and the resulting power output of individual wind turbines.

The location of the wind farm in the wave cycle was an important factor in determining the magnitude of TLW impacts. TLW peaks countered wake losses and TLW troughs enhanced them. There were greater ranges of windspeed and power output during TLW events; the range was greater for TLW trough than peak cases at WMR. Trough windspeeds were, however, coincident with operating points on the power and thrust curves where wake losses were greater. Whether TLW impacts are beneficial, detrimental or balance out will be dependent on: the windfarm location within the TLW wave cycle, windfarm dimensions relative to the TLW wavelength and amplitude, TLW wavelength, TLW amplitude, and TLW orientation in relation to the windfarm dimensions. Whether the wave is quasi-stationary or travelling will also have an impact. A travelling TLW will have transient impacts on turbine outputs that may cancel out overall, whilst quasi-stationary waves may lead to longer term differences compared to predicted power output. Again, the interpretation of TLW impact for all wind farm sizes will largely be determined by what reference conditions the TLW conditions are compared to. For example, when compared to purely neutral conditions, (not existing in reality), TLWs may lead to power output improvements compared to real atmospheric non-TLW situations for the same value of U_N. Without a constant U_N between simulations it was not possible to determine whether there was a balancing effect across the wind farm. Furthermore, it is not yet known whether multiple TLW events at the same windfarm may balance out over a longer period.

5   Future work recommendations

In the current work, it remains unclear how much contribution the following conditions make in TLW situations: (i) Differences in initial U_N, (ii) windspeed recovery from topographical obstacles, (iii) flow adaptation to roughness and temperature changes

after the land-sea transition, (iv) wind farm flow blockage, (v) TLW phase, (vi) height and strength of inversion layer, (vii) presence of surface and/or upper-level stability. Further work to obtain consistent U_N would help quantify influences of the other variables listed above. Whilst subtle differences were found between the stable and neutral surface layer TLW conditions in the current work, applying a variety of surface stability conditions would provide a clearer understanding of the interaction between TLWs and the surface conditions. Further work to determine the relative contributions to wake recovery by the stable surface layer and the capping inversion aloft would need to first address the evolution of the stable surface layer from the inlet to the windfarm. This may be achieved by a considerably longer upstream domain length and exaggerated upstream surface stability. Additionally, varying the inlet wind speed and direction, inversion strength, depth and height, topography dimensions and orientation would help determine their contributions to TLW impacts. It is recommended that future investigations use a variety of windfarm layouts to investigate wake recovery under TLW conditions. Additionally, future investigations into TLWs would benefit from systematic adjustment of wave damping and domain dimension parameters to develop guidelines for optimum wave damping set-up.

In the current work high resolution SCADA data was not available for demonstrating the impact of TLW in a real operational windfarm. Thus, this is a priority for future TLW investigations. For a fuller description of real atmospheric TLW-windfarm interactions moving forward, combined use of CFD, LiDAR, high temporal resolution SCADA and high-resolution mesoscale modelling to downscale ERA5 data is recommended. These methods would enable improved spatial and temporal description of TLW characteristics which could then be utilised to assess the impact of TLWs on wind farms. Assessing different TLWs would provide information on the dependence of impacts on the TLW characteristics. Now theoretical TLW-windfarm impacts have been demonstrated, developing models for larger wind farms and existing wind farm clusters will demonstrate the impact of greater spatial interaction with TLWs. Whilst it may be possible to model a longer domain length in CFD, a coupled micro-mesoscale model would be more appropriate for this large problem. With larger windfarms, a stronger influence on TLW amplitude is expected, which may enhance or reduce the windspeed fluctuations for downstream windfarms.

Code and Data availability

The measurement and reanalysis data used in this paper are open source. ERA5 reanalysis data (ERA5, 2020) are available at https://cds.climate.copernicus.eu/cdsapp#!/home. SAR 10m windfield data are managed by DTU and available at https://science.globalwindatlas.info/. The ANSYS Windmodeller simulations and datainput files are available from the corresponding author on requestat https://github.com/squaroh/WES_TLW.

References

Allaerts, D. and Meyers, J.: Boundary-layer development and gravity waves in conventionally neutral wind farms, J. Fluid Mech., 814, 95–130, https://doi.org/10.1017/jfm.2017.11, 2017a.

Allaerts, D. and Meyers, J.: Gravity Waves and Wind-Farm Efficiency in Neutral and Stable Conditions, Boundary-Layer

680   Meteorol., 166, https://doi.org/10.1007/s10546-017-0307-5, 2017b.

Allaerts, D. and Meyers, J.: Sensitivity and feedback of wind-farm-induced gravity waves, J. Fluid Mech., 862, 990–1028, https://doi.org/10.1017/jfm.2018.969, 2019.

Allaerts, D., Broucke, S. Vanden, Van Lipzig, N., and Meyers, J.: Annual impact of wind-farm gravity waves on the Belgian-Dutch offshore wind-farm cluster, J. Phys. Conf. Ser., 1037, https://doi.org/10.1088/1742-6596/1037/7/072006, 2018.

685   ANSYS: ANSYS CFX Solver Theory Guidem Version 18.0, 2017.

Argyle, P.: Computational fluid dynamics modelling of wind turbine wake losses in large offshore wind farms , incorporating atmospheric stability, Loughborough University, 2014.

Chunchuzov, I., Vachon, P. W., and Li, X.: Analysis and Modeling of Atmospheric Gravity Waves Observed in RADARSAT SAR Images, Remote Sens. Environ., 74, 343–361, https://doi.org/http://dx.doi.org/10.1016/S0034-4257(00)00076-6, 2000.

690   ERA5: https://cds.climate.copernicus.eu/cdsapp#!/home, last access: 24 July 2020.

Draxl, C., Worsnop, R. P., Xia, G., Pichugina, Y., Chand, D., Lundquist, J. K., Sharp, J., Wedam, G., Wilczak, J. M., and Berg, L. K.: Mountain waves can impact wind power generation, Wind Energy Sci., 6, 45–60, https://doi.org/10.5194/wes-6-45-2021, 2021.

DTU Wind Energy: ENVISAT and Sentinel 1 surface wind field processing,: https://satwinds.windenergy.dtu.dk/, 2016./.

695   DTU Wind Energy: Global Winds Atlas (GWA) science portal, https://science.globalwindatlas.info/, 2021.

Durran, D. R. and Klemp, J. B.: A Compressible Model for the Simulation of Moist Mountain Waves, Mon. Weather Rev., 111, 2341–2361, https://doi.org/10.1175/1520-0493(1983)111<2341:ACMFTS>2.0.CO;2, 1983.

Gadde, S. N. and Stevens, R. J. A. M.: Effect of Coriolis force on a wind farm wake, J. Phys. Conf. Ser., 1256, https://doi.org/10.1088/1742-6596/1256/1/012026, 2019.

700   Garratt, J. R.: Appendix 3, in: The atmospheric boundary layer, Cambridge atmospheric and space science series. Cambridge University Press, Cambridge, UK, 1994.

Gossard, E. E. and Hooke, W. H.: Waves in the atmosphere : atmospheric infrasound and gravity waves : their generation and propagation, Amsterdam ; New York : Elsevier Scientific Pub. Co., 1975.

Haupt, S. E., Berg, L. K., Decastro, A., Gagne, D. J., Jimenez, P., Juliano, T., Kosovic, B., Mirocha, J. D., Quon, E., Sauer, J.,

705   Allaerts, D., Churchfield, M. J., Draxl, C., Hawbecker, P., Jonko, A., Kaul, C. M., McCandless, T., Munoz-Esparza, D., Rai, R. K., and Shaw, W. J.: FY 2019 Report of the Atmosphere to Electrons Mesoscale-to-Microscale Coupling Project, Alexandria, https://doi.org/10.2172/1735568, 2019.

Hills, M. O. G. and Durran, D. R.: Nonstationary Trapped Lee Waves Generated by the Passage of an Isolated Jet, J. Atmos. Sci., 69, 3040–3059, https://doi.org/10.1175/JAS-D-12-047.1, 2012.

710   Jia, M., Yuan, J., Wang, C., Xia, H., Wu, Y., Zhao, L., Wei, T., Wu, J., Wang, L., Gu, S.-Y., Liu, L., Lu, D., Chen, R., Xue, X., and Dou, X.: Long-live High Frequency Gravity Waves in Atmospheric Boundary Layer: Observations and Simulations, https://doi.org/10.5194/acp-2019-256, 2019.

Klemp, J. B. and Lilly, D. K.: Numerical Simulation of Hydrostatic Mountain Waves, J. Atmos. Sci., 35, 78–107, https://doi.org/10.1175/1520-0469(1978)035<0078:NSOHMW>2.0.CO;2, 1978.

715 Lanzilao, L. and Meyers, J.: Set-point optimization in wind farms to mitigate effects of flow blockage induced by gravity waves, 1–30, 2020.

Lanzilao, L. and Meyers, J.: Set-point optimization in wind farms to mitigate effects of flow blockage induced by atmospheric gravity waves, Wind Energy Sci., 6, 247–271, https://doi.org/10.5194/wes-6-247-2021, 2021.

Li, L., Chan, P. W., Zhang, L., and Hu, F.: Numerical Simulation of a Lee Wave Case over Three-Dimensional Mountainous
720 Terrain under Strong Wind Condition, Adv. Meteorol., https://doi.org/http://dx.doi.org/10.1155/2013/304321, 2013a.

Li, X.: Atmospheric Vortex Streets and Gravity Waves, in: SAR Marine User's Manual, 341–354, 2004.

Li, X., Zheng, W., Yang, X., Zhang, J. A., Pichel, W. G., and Li, Z.: Coexistence of Atmospheric Gravity Waves and Boundary Layer Rolls Observed by SAR*, J. Atmos. Sci., 70, 3448–3459, 2013b.

Maas, O. and Raasch, S.: Wake properties and power output of very large wind farms for different meteorological conditions
725 and turbine spacings: a large-eddy simulation case study for the German Bight, Wind Energy Sci., 7, 715–739, https://doi.org/10.5194/wes-7-715-2022, 2022.

Montavon, C.: Windmodeller customisation, 2017.

Montavon, C., Jones I, and Wells, A. K.: D3 Final Report: Modelling Offshore Wind Farms using CFD, Carbon Trust Report, OWA Phase II, 2012.

730 Montavon, C. A., Hui, S., Graham, J., Malins, D., Housley, P., Dahl, E., de Villierts, P., and Gribben, B.: Offshore Wind Accelerator: Wake Modelling Using CFD, in: European Wind Energy Association Conference and Exhibition, 2011.

Nappo, C. J.: Mountain Waves, in: International Geophysics, vol. 102, Academic Press, 57–85, https://doi.org/10.1016/B978-0-12-385223-6.00003-3, 2012.

Ollier, S. J., Watson, S. J., and Montavon, C.: Atmospheric gravity wave impacts on an offshore wind farm, IOP Conf. Ser. J.
735 Phys., 1037, https://doi.org/doi :10.1088/1742-6596/1037/7/072050, 2018.

Rasmussen, E. A. and Aakjær, P. D.: Two Polar Lows Affecting Denmark, 47, 326–338, https://doi.org/10.1002/j.1477-8696.1992.tb07196.x, 1992.

Romanova, N. N. and Yakushkin, I. G.: Internal gravity waves in the lower atmosphere and sources of their generation (review), Ocean. Phys. C/C, 31, 151–172, 1995.

740 Smith, R. B.: Gravity wave effects on wind farm efficiency, Wind Energy, 13, 449–458, https://doi.org/10.1002/we.366, 2010.

Thomson, R. E., Vachon, P. W., and Borstad, G. A.: Airborne synthetic aperture radar imagery of atmospheric gravity waves, J. Geophys. Res. Ocean., 97, 14249–14257, https://doi.org/10.1029/92JC01178, 1992.

Vachon, P. W., Johannessen, O. M., and Johannessen, J. A.: An ERS 1 synthetic aperture radar image of atmospheric lee waves, J. Geophys. Res. Ocean., 99, 22483–22490, https://doi.org/10.1029/94JC01392, 1994.

745 Vosper, S. B., Ross, A. N., Renfrew, I. A., Sheridan, P., Elvidge, A. D., and Grubišić, V.: Current Challenges in Orographic Flow Dynamics: Turbulent Exchange Due to Low-Level Gravity-Wave Processes, Atmosphere (Basel)., 9,

https://doi.org/10.3390/atmos9090361, 2018.

Warner, T. T.: Numerical Weather and Climate Prediction, Cambridge University Press, https://doi.org/10.1017/CBO9780511763243, 2010.

750 Wilczak, J. M., Stoelinga, M., Berg, L. K., Sharp, J., Draxl, C., McCaffrey, K., Banta, R. M., Bianco, L., Djalalova, I., Lundquist, J. K., Muradyan, P., Choukulkar, A., Leo, L., Bonin, T., Pichugina, Y., Eckman, R., Long, C. N., Lantz, K., Worsnop, R. P., Bickford, J., Bodini, N., Chand, D., Clifton, A., Cline, J., Cook, D. R., Fernando, H. J. S., Friedrich, K., Krishnamurthy, R., Marquis, M., McCaa, J., Olson, J. B., Otarola-Bustos, S., Scott, G., Shaw, W. J., Wharton, S., and White, A. B.: The Second Wind Forecast Improvement Project (WFIP2): Observational Field Campaign, Bull. Am. Meteorol. Soc.,

755 100, 1701–1723, https://doi.org/10.1175/BAMS-D-18-0035.1, 2019.

Wu, K. L. and Porté-Agel, F.: Flow Adjustment Inside and Around Large Finite-Size Wind Farms, 10, 2017.

Xia, G., Draxl, C., Raghavendra, A., and Lundquist, J. K.: Validating simulated mountain wave impacts on hub-height wind speed using SoDAR observations, Renew. Energy, 163, 2220–2230, https://doi.org/https://doi.org/10.1016/j.renene.2020.10.127, 2021.

760 Xu, Q., Li, X., Bao, S., and Pietrafesa, L. J.: SAR Observation and Numerical Simulation of Mountain Lee Waves Near Kuril Islands Forced by an Extratropical Cyclone, IEEE Trans. Geosci. Remote Sens., 1–9, https://doi.org/10.1109/TGRS.2016.2596678, 2016.

Allaerts, D. and Meyers, J.: Boundary-layer development and gravity waves in conventionally neutral wind farms, J. Fluid Mech., 814, 95–130, https://doi.org/10.1017/jfm.2017.11, 2017a.

765 Allaerts, D. and Meyers, J.: Gravity Waves and Wind-Farm Efficiency in Neutral and Stable Conditions, Boundary-Layer Meteorol., 166, https://doi.org/10.1007/s10546-017-0307-5, 2017b.

Allaerts, D. and Meyers, J.: Sensitivity and feedback of wind-farm-induced gravity waves, J. Fluid Mech., 862, 990–1028, https://doi.org/10.1017/jfm.2018.969, 2019.

Allaerts, D., Broucke, S. Vanden, Van Lipzig, N., and Meyers, J.: Annual impact of wind-farm gravity waves on the Belgian-

770 Dutch offshore wind-farm cluster, J. Phys. Conf. Ser., 1037, https://doi.org/10.1088/1742-6596/1037/7/072006, 2018.

ANSYS: ANSYS CFX Solver Theory Guidem Version 18.0, 2017.

Argyle, P.: Computational fluid dynamics modelling of wind turbine wake losses in large offshore wind farms , incorporating atmospheric stability, Loughborough University, 2014.

Chunchuzov, I., Vachon, P. W., and Li, X.: Analysis and Modeling of Atmospheric Gravity Waves Observed in RADARSAT

775 SAR Images, Remote Sens. Environ., 74, 343–361, https://doi.org/http://dx.doi.org/10.1016/S0034-4257(00)00076-6, 2000.

ERA5: https://cds.climate.copernicus.eu/cdsapp#!/home, last access: 24 July 2020.

Draxl, C., Worsnop, R. P., Xia, G., Pichugina, Y., Chand, D., Lundquist, J. K., Sharp, J., Wedam, G., Wilczak, J. M., and Berg, L. K.: Mountain waves can impact wind power generation, Wind Energy Sci., 6, 45–60, https://doi.org/10.5194/wes-6-45-2021, 2021.

780 DTU Wind Energy: ENVISAT and Sentinel 1 surface wind field processing,: https://satwinds.windenergy.dtu.dk/, 2016./.

48

DTU Wind Energy: Global Winds Atlas (GWA) science portal, https://science.globalwindatlas.info/, 2021.

Durran, D. R. and Klemp, J. B.: A Compressible Model for the Simulation of Moist Mountain Waves, Mon. Weather Rev., 111, 2341–2361, https://doi.org/10.1175/1520-0493(1983)111<2341:ACMFTS>2.0.CO;2, 1983.

Gadde, S. N. and Stevens, R. J. A. M.: Effect of Coriolis force on a wind farm wake, J. Phys. Conf. Ser., 1256, https://doi.org/10.1088/1742-6596/1256/1/012026, 2019.

Garratt, J. R.: Appendix 3, in: The atmospheric boundary layer, Cambridge atmospheric and space science series. Cambridge University Press, Cambridge, UK, 1994.

Gossard, E. E. and Hooke, W. H.: Waves in the atmosphere : atmospheric infrasound and gravity waves : their generation and propagation, Amsterdam ; New York : Elsevier Scientific Pub. Co., 1975.

Haupt, S. E., Berg, L. K., Decastro, A., Gagne, D. J., Jimenez, P., Juliano, T., Kosovic, B., Mirocha, J. D., Quon, E., Sauer, J., Allaerts, D., Churchfield, M. J., Draxl, C., Hawbecker, P., Jonko, A., Kaul, C. M., McCandless, T., Munoz-Esparza, D., Rai, R. K., and Shaw, W. J.: FY 2019 Report of the Atmosphere to Electrons Mesoscale-to-Microscale Coupling Project, Alexandria, https://doi.org/10.2172/1735568, 2019.

Hills, M. O. G. and Durran, D. R.: Nonstationary Trapped Lee Waves Generated by the Passage of an Isolated Jet, J. Atmos. Sci., 69, 3040–3059, https://doi.org/10.1175/JAS-D-12-047.1, 2012.

Jia, M., Yuan, J., Wang, C., Xia, H., Wu, Y., Zhao, L., Wei, T., Wu, J., Wang, L., Gu, S.-Y., Liu, L., Lu, D., Chen, R., Xue, X., and Dou, X.: Long-live High Frequency Gravity Waves in Atmospheric Boundary Layer: Observations and Simulations, https://doi.org/10.5194/acp-2019-256, 2019.

Klemp, J. B. and Lilly, D. K.: Numerical Simulation of Hydrostatic Mountain Waves, J. Atmos. Sci., 35, 78–107, https://doi.org/10.1175/1520-0469(1978)035<0078:NSOHMW>2.0.CO;2, 1978.

Lanzilao, L. and Meyers, J.: Set-point optimization in wind farms to mitigate effects of flow blockage induced by gravity waves, 1–30, 2020.

Lanzilao, L. and Meyers, J.: Set-point optimization in wind farms to mitigate effects of flow blockage induced by atmospheric gravity waves, Wind Energy Sci., 6, 247–271, https://doi.org/10.5194/wes-6-247-2021, 2021.

Li, L., Chan, P. W., Zhang, L., and Hu, F.: Numerical Simulation of a Lee Wave Case over Three-Dimensional Mountainous Terrain under Strong Wind Condition, Adv. Meteorol., https://doi.org/http://dx.doi.org/10.1155/2013/304321, 2013a.

Li, X.: Atmospheric Vortex Streets and Gravity Waves, in: SAR Marine User's Manual, 341–354, 2004.

Li, X., Zheng, W., Yang, X., Zhang, J. A., Pichel, W. G., and Li, Z.: Coexistence of Atmospheric Gravity Waves and Boundary Layer Rolls Observed by SAR*, J. Atmos. Sci., 70, 3448–3459, 2013b.

Maas, O. and Raasch, S.: Wake properties and power output of very large wind farms for different meteorological conditions and turbine spacings: a large-eddy simulation case study for the German Bight, Wind Energy Sci., 7, 715–739, https://doi.org/10.5194/wes-7-715-2022, 2022.

Montavon, C.: Windmodeller customisation, 2017.

Montavon, C., Jones I, and Wells, A. K.: D3 Final Report: Modelling Offshore Wind Farms using CFD, Carbon Trust Report,

815 OWA Phase II, 2012.

Montavon, C. A., Hui, S., Graham, J., Malins, D., Housley, P., Dahl, E., de Villierts, P., and Gribben, B.: Offshore Wind Accelerator: Wake Modelling Using CFD, in: European Wind Energy Association Conference and Exhibition, 2011.

Nappo, C. J.: Mountain Waves, in: International Geophysics, vol. 102, Academic Press, 57–85, https://doi.org/10.1016/B978-0-12-385223-6.00003-3, 2012.

820 Ollier, S. J., Watson, S. J., and Montavon, C.: Atmospheric gravity wave impacts on an offshore wind farm, IOP Conf. Ser. J. Phys., 1037, https://doi.org/doi :10.1088/1742-6596/1037/7/072050, 2018.

Rasmussen, E. A. and Aakjær, P. D.: Two Polar Lows Affecting Denmark, 47, 326–338, https://doi.org/10.1002/j.1477-8696.1992.tb07196.x, 1992.

Romanova, N. N. and Yakushkin, I. G.: Internal gravity waves in the lower atmosphere and sources of their generation

825 (review), Ocean. Phys. C/C, 31, 151–172, 1995.

Smith, R. B.: Gravity wave effects on wind farm efficiency, Wind Energy, 13, 449–458, https://doi.org/10.1002/we.366, 2010.

Thomson, R. E., Vachon, P. W., and Borstad, G. A.: Airborne synthetic aperture radar imagery of atmospheric gravity waves, J. Geophys. Res. Ocean., 97, 14249–14257, https://doi.org/10.1029/92JC01178, 1992.

Vachon, P. W., Johannessen, O. M., and Johannessen, J. A.: An ERS 1 synthetic aperture radar image of atmospheric lee

830 waves, J. Geophys. Res. Ocean., 99, 22483–22490, https://doi.org/10.1029/94JC01392, 1994.

Vosper, S. B., Ross, A. N., Renfrew, I. A., Sheridan, P., Elvidge, A. D., and Grubišić, V.: Current Challenges in Orographic Flow Dynamics: Turbulent Exchange Due to Low-Level Gravity-Wave Processes, Atmosphere (Basel)., 9, https://doi.org/10.3390/atmos9090361, 2018.

Warner, T. T.: Numerical Weather and Climate Prediction, Cambridge University Press,

835 https://doi.org/10.1017/CBO9780511763243, 2010.

Wilczak, J. M., Stoelinga, M., Berg, L. K., Sharp, J., Draxl, C., McCaffrey, K., Banta, R. M., Bianco, L., Djalalova, I., Lundquist, J. K., Muradyan, P., Choukulkar, A., Leo, L., Bonin, T., Pichugina, Y., Eckman, R., Long, C. N., Lantz, K., Worsnop, R. P., Bickford, J., Bodini, N., Chand, D., Clifton, A., Cline, J., Cook, D. R., Fernando, H. J. S., Friedrich, K., Krishnamurthy, R., Marquis, M., McCaa, J., Olson, J. B., Otarola-Bustos, S., Scott, G., Shaw, W. J., Wharton, S., and White,

840 A. B.: The Second Wind Forecast Improvement Project (WFIP2): Observational Field Campaign, Bull. Am. Meteorol. Soc., 100, 1701–1723, https://doi.org/10.1175/BAMS-D-18-0035.1, 2019.

Wu, K. L. and Porté-Agel, F.: Flow Adjustment Inside and Around Large Finite-Size Wind Farms, 10, 2017.

Xia, G., Draxl, C., Raghavendra, A., and Lundquist, J. K.: Validating simulated mountain wave impacts on hub-height wind speed using SoDAR observations, Renew. Energy, 163, 2220–2230,

845 https://doi.org/https://doi.org/10.1016/j.renene.2020.10.127, 2021.

Xu, Q., Li, X., Bao, S., and Pietrafesa, L. J.: SAR Observation and Numerical Simulation of Mountain Lee Waves Near Kuril Islands Forced by an Extratropical Cyclone, IEEE Trans. Geosci. Remote Sens., 1–9, https://doi.org/10.1109/TGRS.2016.2596678, 2016.
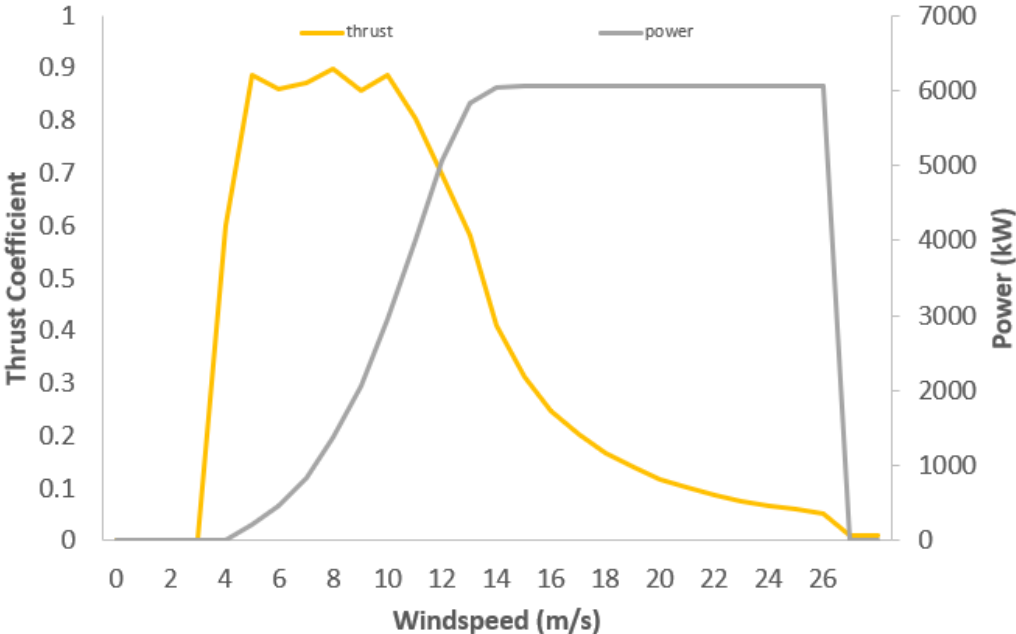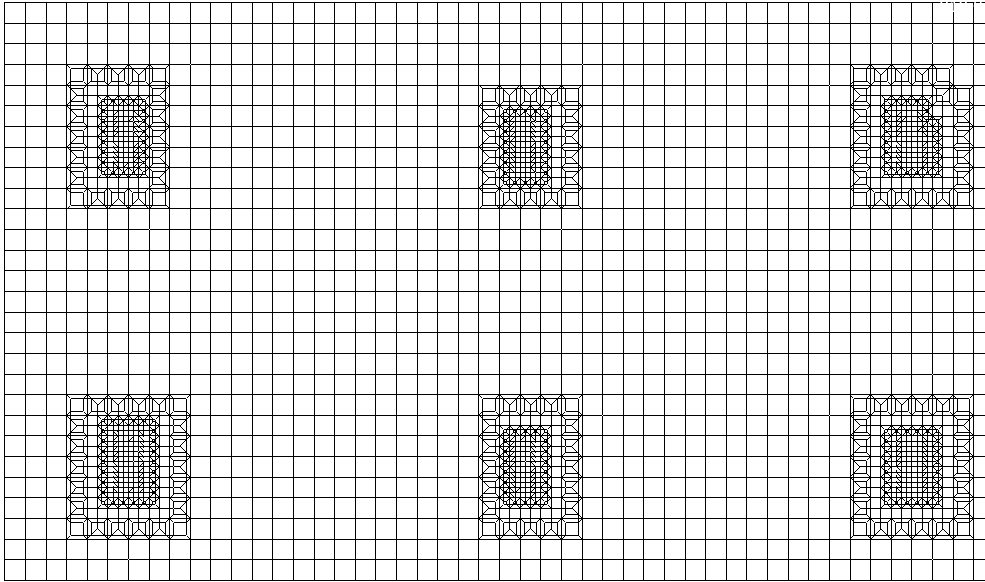
850   **Appendix A**

Figure A. 1. Thrust coefficient and power curve data used for the 6MW 154m diameter turbines in the simulations

Appendix B

Figure B. 1. Horizontal mesh structure for the WMR wind farm region of simulation domain at turbine hub height (106 m) used for all simulations. The mesh refinement around each actuator disk is shown in the darker regions. Note that mesh refinement around individual turbines leads to asymmetrical meshes for some turbines.

Appendix C

Fig. C. 1 shows the shear exponent factor (α) for the neutral case (r0Nh-WMR) and the TLW case with a neutral surface layer (r7Nh-WMR). Shear is more variable within the TLW case where there are deeper near-wake losses (Fig. C. 2, Fig. C. 3). The greatest shear variability is experienced by F01 and F07 which experience the deepest near-wake losses and TI (Fig. C. 3) due to having a full column of turbines upstream. For the TLW case the wakes and elevated wake TI persist further downstream into the wave damping region. The impact of the TLW and the capping inversion are coupled so it is unclear which has a greater influence on the shear, turbulence and near wake loss depth is unclear.
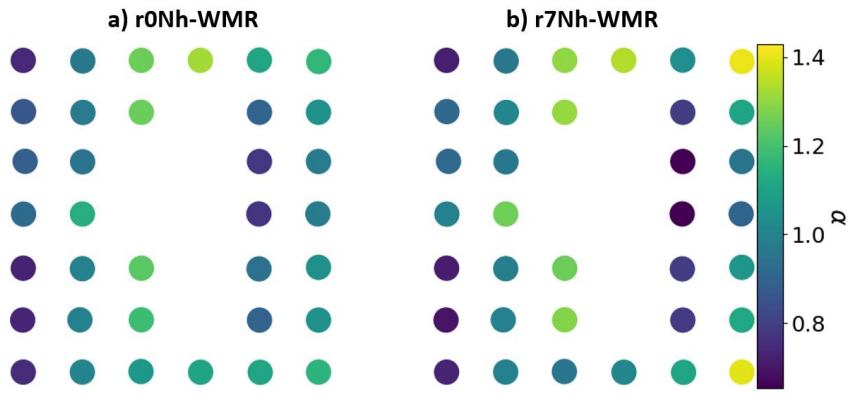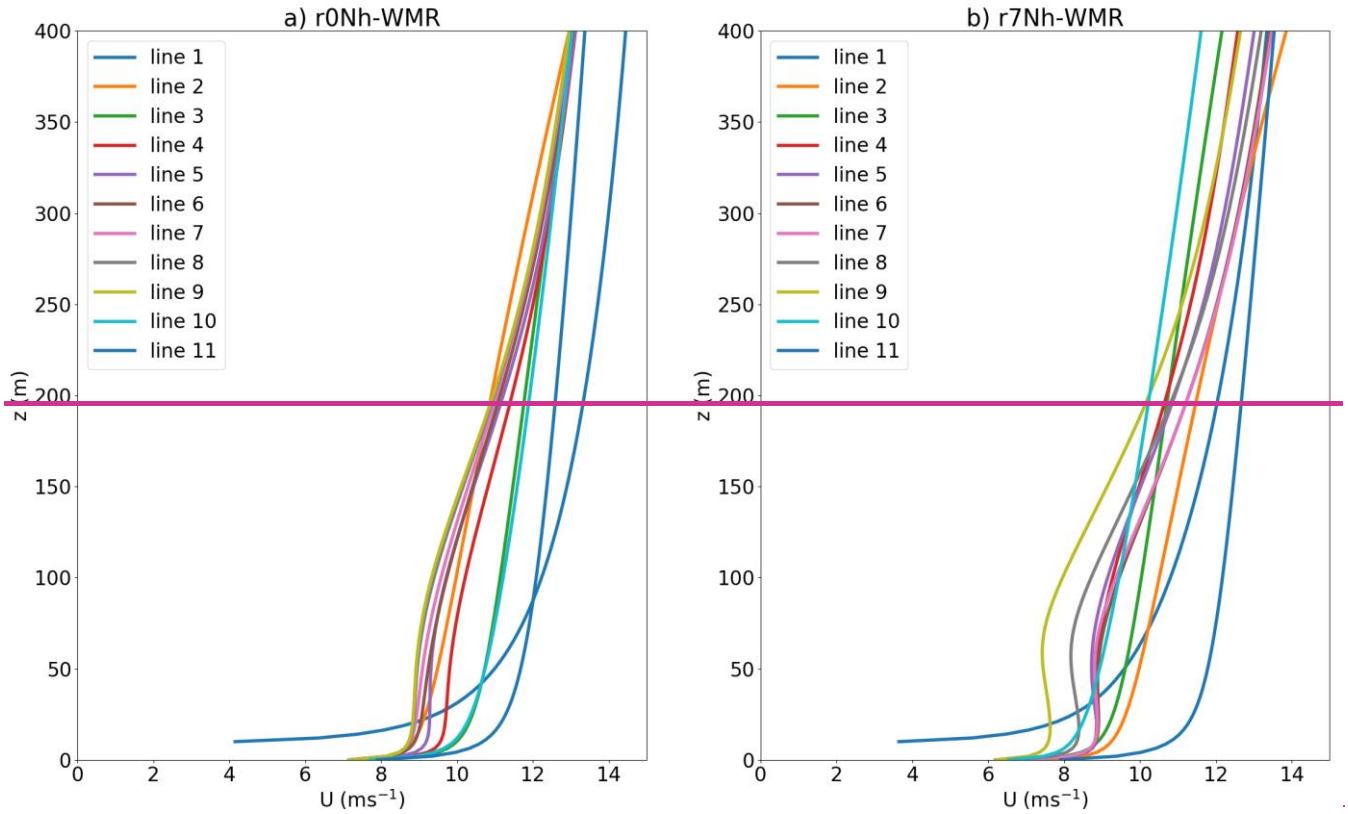
52

Figure C. 1. WMR view from above - shear exponent factor (α) for a) r7Nh-WMR and b) r0Nh-WMR.
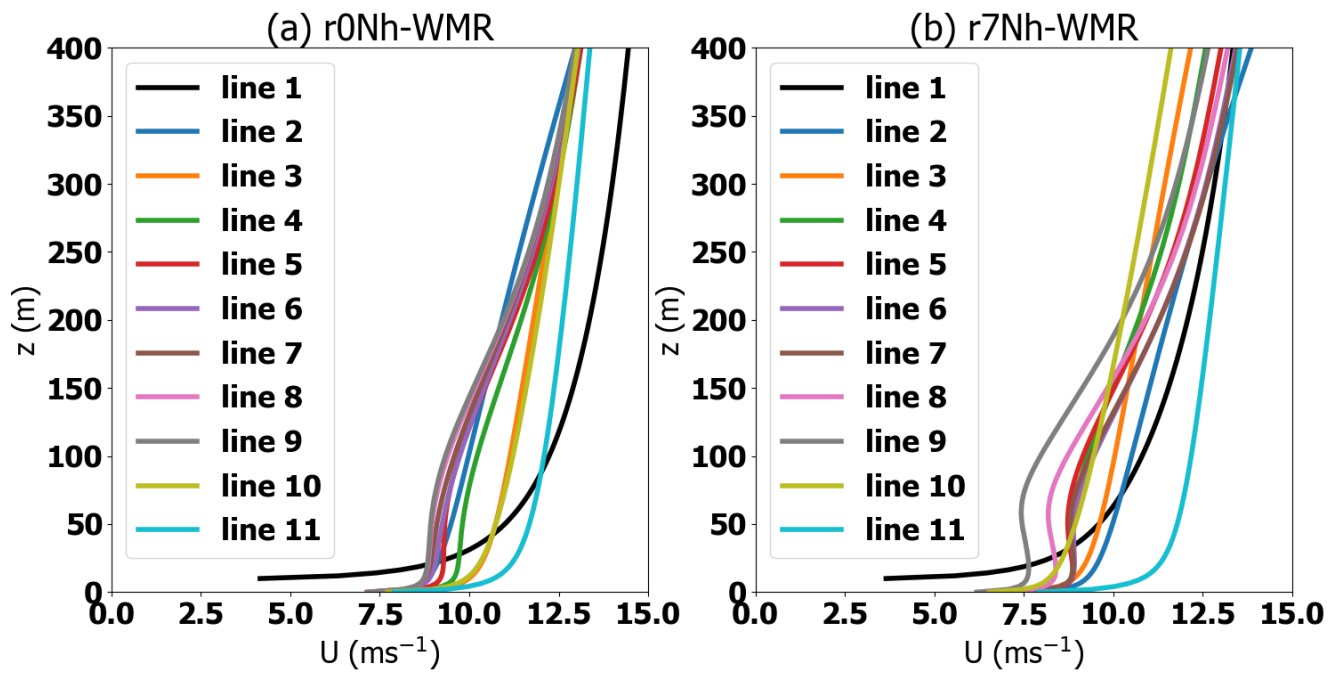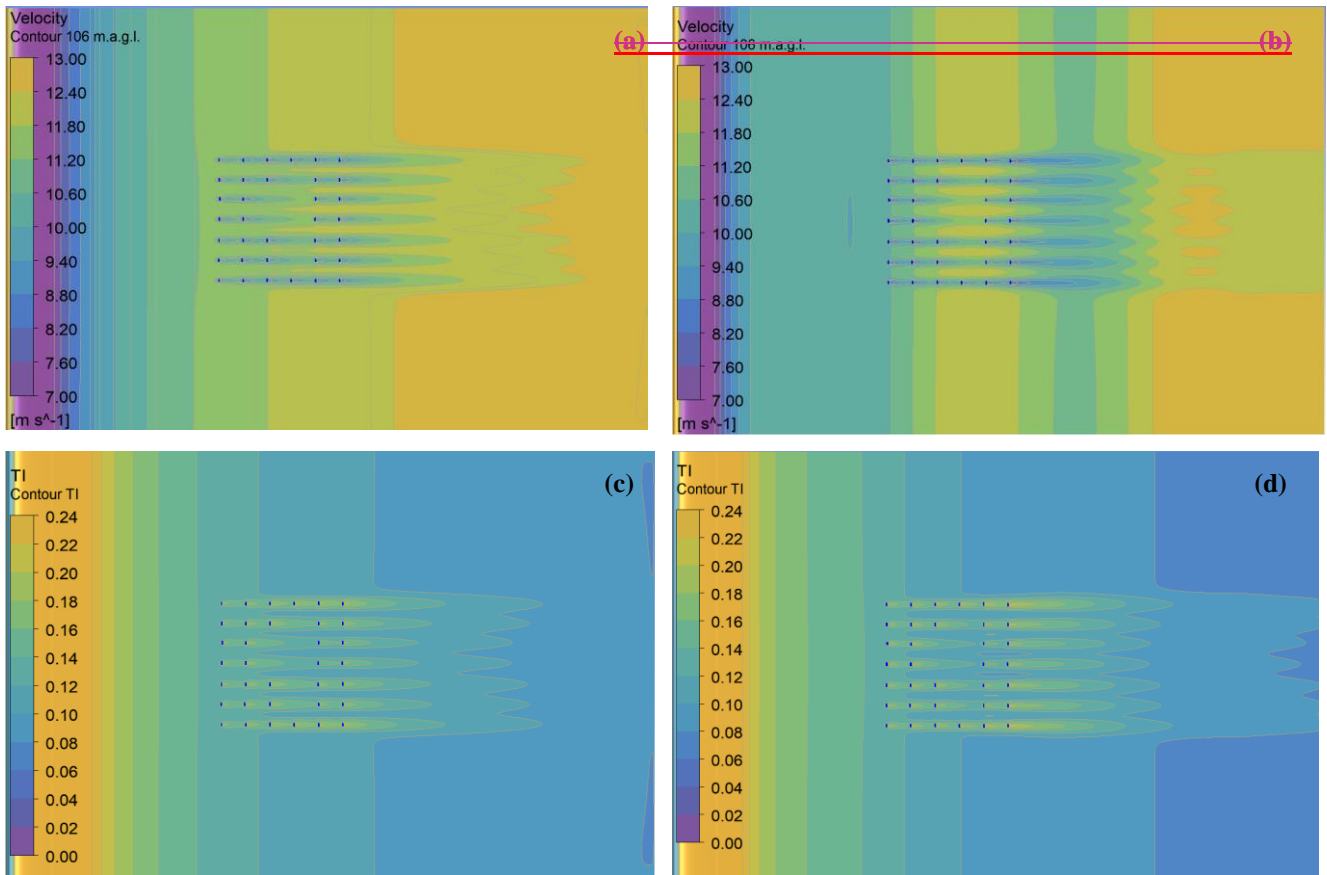
870

Figure C. 2. Vertical windspeed profiles for a) r0Nh-WMR and b) r7Nh-WMR. Numbered lines correspond to lines 1-11 labelled in Fig. 13a.

875 **Figure C. 3. WMR view from above in the CFD domain with colour contours of 106 m hub height windspeeds and TI for a), c) r0Nh-WMR and b), d) r 7Nh-WMR, see legend for windspeeds.**